

UPPSALA
UNIVERSITET

Digital Comprehensive Summaries of Uppsala Dissertations from the Faculty of Science and Technology 892

Materials Development for Solid-State Dye-Sensitized Solar Cells

MARTIN KARLSSON



ACTA
UNIVERSITATIS
UPSALIENSIS
UPPSALA
2012

ISSN 1651-6214
ISBN 978-91-554-8255-8
urn:nbn:se:uu:diva-165458

Dissertation presented at Uppsala University to be publicly examined in Polhemssalen, Ångströmlaboratoriet, Lägerhyddsvägen 1, Uppsala. Friday, February 24, 2012 at 10:00 for the degree of Doctor of Philosophy. The examination will be conducted in English.

Abstract

Karlsson, M. 2012. Materials Development for Solid-State Dye-Sensitized Solar Cells. Acta Universitatis Upsaliensis. *Digital Comprehensive Summaries of Uppsala Dissertations from the Faculty of Science and Technology* 892. 89 pp. Uppsala. ISBN 978-91-554-8255-8.

The dye-sensitized solar cell (DSC) is a photovoltaic technology with the potential to efficiently and economically harvest and convert energy from the sun to electrical power. DSCs are built using abundant and low cost materials such as titanium dioxide (TiO_2) and organic dye molecules. The dye molecule acts as a light absorber funneling electrons from its photo-excited state to the TiO_2. A redox mediator which typical consists of iodide/tri-iodide undergoes redox reactions at the counter electrode and the oxidized dye molecule creating a circuit between the two. Solid-state versions of the DSC are also being investigated. In these devices the liquid electrolyte is exchanged with solid hole transporting material in order to both simplify the solar cell production as well as increasing the open-circuit potential and stability of the solar cell. One main draw-back, which limits the increase in conversion efficiency of solid-state DSC is the faster electron recombination dynamics between electrons in the TiO_2 and holes in the solid hole transporter. Currently the highest performing liquid electrolyte DSC reaches a conversion efficiency of over 12 %, while the solid-state DSC is tailing with 7 %.

Materials development is crucial for further development of the DSC technology, hopefully leading to better stability and higher efficiency. Many types of dye molecules, redox mediators as well as hole transporting materials and working electrode materials have all been tested and modified in the past in order to improve DSC performance. Significant further improvement of DSC technology requires a better understanding of the operating principle behind the DSC and the interaction between the different components. This requires advanced characterization methods for materials and solar cells. In this thesis, new materials for DSC have been developed, tested and characterized using advanced methods.

Atomic layer deposition was employed to develop a new working electrodes based on the core-shell SnO_2-TiO_2 material. These working electrodes were successfully used in both liquid and solid-state DSC to decrease the electron recombination dynamics and increase conversion efficiencies. The molecular structure of sensitizing dyes also plays a major role in electron recombination. Thus, investigating different molecular structures of sensitizing dyes is of importance when trying to improve DSC performance. Seven new molecular dye structures based on three different chromophore units were investigated in both liquid electrolyte and solid-state DSC. For example, adding a second anchoring group on the D35 molecular structure improved the light harvesting capabilities of the dye but did not result in DSC devices with higher conversion efficiency. Increasing the bulkiness of the molecular dye structure facing away from the TiO_2 surface yielded on the other hand higher both slower electron recombination and higher conversion efficiencies.

The effects of oxygen on solid-state DSC using spiro-OMeTAD were also studied. The chemical oxidation of the solid-state hole transporting material was found to depend on both time and storing conditions of the complete DSC devices. Solar cells with higher conversion efficiency were found for solid-state DSC stored under ambient air conditions before measured.

Finally, a novel and efficient organic tandem solar cell was demonstrated built using a solid-state DSC and a bulk heterojunction solar. The 6 % efficient tandem cell almost perfectly added the photo-potentials of the subcells together while keeping the photo-current intact.

Martin Karlsson, Uppsala University, Department of Physical and Analytical Chemistry, Physical Chemistry, Box 577, SE-751 23 Uppsala, Sweden.

© Martin Karlsson 2012

ISSN 1651-6214
ISBN 978-91-554-8255-8
urn:nbn:se:uu:diva-165458 (http://urn.kb.se/resolve?urn=urn:nbn:se:uu:diva-165458)

“Good work and keep on going”
- Note to myself

List of Papers

This thesis is based on the following papers, which are referred to in the text by their Roman numerals.

I Karlsson, M., Jõrgi, I., Eriksson, S. K., Bosman, M. Rensmo, H., Boman, M., Hagfeldt, A., Boschloo, G. Dye-sensitized solar cells employing a SnO_2-TiO_2 core-shell structure made by atomic layer deposition.
Submitted to Advanced Energy Materials

II Jiang, X., Karlsson, K. M., Gabrielsson, E., Johansson, E. M. J., Quintana, M., Karlsson, M., Sun, L., Boschloo, G., Hagfeldt, A. (2011) Highly efficient solid-state dye-sensitized solar cells based on triphenylamine dyes. Advanced Functional Materials, 21(15):2944-2952

III Cappel, U., Karlsson, M. H., Pschirer, N. G., Eickemeyer, F., Schöneboom, J., Erk, P., Boschloo, G., Hagfeldt, A. (2009) A broadly absorbing perylene dye for solid-state dye-sensitized solar cells. Journal of Physical Chemistry C, 113(33):14595-14597

IV Karlsson, M., Yang, L., Karlsson, K. M., Sun, L., Boschloo, G., Hagfeldt, A. Phenoxazine dyes in solid-state dye-sensitized solar cells. *Submitted to Journal of Photochemistry and Photobiology A: Chemistry*

V Karlsson, M., Rensmo, H., Boschloo, G., Hagfeldt, A. Effects of oxygen in solid-state dye-sensitized solar cells. *In Manuscript*

VI Bruder, I., Karlsson, M., Eickemeyer, F., Hwang, J., Erk, P., Hagfeldt, A., Weis, J., Pschirer, N. (2009) Efficient organic tandem cell combining a solid-state dye-sensitized and a vacuum deposited bulk heterojunction solar cell. *Solar Energy Materials & Solar Cells,* 93(10):1896-1899

Reprints were made with permission from the respective publishers.

Comments on contribution for the above mentioned papers
I was the main responsible person for *Papers I, IV* and *V,* for which I carried out most of the solar cell characterization, material preparation and wrote the manuscripts. ALD was made by Indrek Jõgi and XPS measurement by Susanna Eriksson. For *Paper II* and *III* I was involved in the optimization of the solar cells and the materials as well as in the discussion of the manuscripts. The contributions to paper VI were shared between Ingmar Bruder and myself. I made the DSC part of the tandem cell and most of the device characterization and wrote half of the manuscript. I did not synthesize any organic material or perform any quantum mechanical calculations.

I am a co-author of the following papers/patents which are not included in this thesis:

- Yang, L., Cappel, U. B., Unger, E. L., Karlsson, M., Karlsson, K. M., Gabrielsson, E., Sun, L., Boschloo, G., Hagfeldt, A., Johansson, E. M. J. (2012) Comparing spiro-OMeTAD and P3HT hole conductors in efficient solid state dye-sensitized solar cells. *Physical Chemistry Chemical Physics*, 14:779-789

- Photovoltaic tandem cell.
  Patent publication number: WO/2009/013282

Content

1. Introduction 13
1.1 Motivation 13
1.2 Energy from the sun 14
1.3 Overview of the photovoltaic concepts 15
1.3.1 History of inorganic solar cells 15
1.3.2 Organic photovoltaics 15
1.3.3 Photoelectrochemical cells 17
1.5 Aim of the thesis 19

2. Materials for the dye-sensitized solar cells 20
2.1 The working electrode 20
2.1.1 TiO_2 blocking layers made by spray pyrolysis 21
2.2 The light absorbing material 23
2.3 Electrolyte/Hole transporting material 26
2.4 Solar cell additives 28
2.5 Counter electrode 29

3. The operation of the dye-sensitized solar cells 31
3.1 Electron transfer steps in dye-sensitized solar cells 35
3.1.1 Diffusion processes 35
3.2 Charge transfer processes in solid-state DSC 37
3.3 Obstacles for increasing conversion efficiency in dye-sensitized solar cells 40
3.4 Stability of dye-sensitized solar cells 43

4. Methods 44
4.1 Solar cell preparation and assembly 44
4.1.1 Liquid electrolyte dye-sensitized solar cells 44
4.1.2 Solid-state dye-sensitized solar cells 45
4.1.3 A sDSC and bulk heterojunction tandem device 46
4.2. Preparation of Materials for DSC 47
4.2.1 Colloidal metal oxide particles for DSC 47
4.2.2 Core-shell structures by atomic layer deposition 48
4.3 Characterization of complete solar cells 50
4.3.1 Current – Voltage (J-V) Measurement 50
4.3.2 Incident-photon-to-current-conversion-efficiency 52
4.3.3 Electron lifetime measurements 53

4.3.4 Electron transport measurements 54
4.3.5 Charge extraction techniques 56
4.3.6 Impedance spectroscopy (EIS) 56
4.4 Characterization of solar cell materials 58
4.4.1 Optical measurements (UV-VIS) 58
4.4.2 Electrochemistry 58
4.4.3 Conductivity measurements on IME 60
4.4.3 Carrier mobility using time-of-flight 61

5. Results 63
5.1 Core-shell structures for DSC (*Paper I*) 64
5.2 Efficient dyes for DSC (*Paper II*) 66
5.3 A perylene dye in liquid and solid-state DSC (*Paper III*) 69
5.4 Phenoxazine dyes for sDSC (*Paper IV*) 70
5.5 Effects of oxygen in sDSC (*Paper V*) 72
5.6 Tandem bulk heterojunction – solid-state DSC (*Paper VI*) 74

6. Concluding remarks 77

Sammanfattning på svenska 78

Acknowledgement 82

References 83

Abbreviations

AM	Air mass density
APCE(λ)	Absorbed-photon-to-current-conversion-efficiency
ALD	Atomic layer deposition
BHJ	Bulk heterojunction
Biphen	Phenanthroline
C_{60}	Fullerene-C60
C_{FTO}	Electrostatic capacitance of the FTO/electrolyte interface
C_{Pt}	Interfacial capacitance at the counter electrode
CV	Cyclic voltammetry
C_{μ}	The chemical capacitance of the TiO_2
D_n	Effective electron diffusion coefficient
e	Electron charge
E_{cb}	Conduction band potential
E_{fb}	Flat band potential
$E_{F,n}$	Electron Fermi energy
$E^*_{F,n}$	Electron quasi-Fermi energy
$F^*_{F,p}$	Hole quasi-Fermi energy
$E_{F,redox}$	Reduction-oxidation energy
EIS	Electrical impedance spectroscopy
$E^{\circ\prime}_{(D^+/D)}$	Oxidation potential
$E^{\circ\prime}_{(D/D^-)}$	Reduction potential
eV	Electronvolt
E(λ)	Photon flux energy density
FF	Fill factor
FTO	Fluorine doped tin dioxide
HTM	Hole transporting material
HOMO	Highest occupied molecular orbital
I_0	Light intensity

IME	Interdigitated micro-electrodes
IPCE(λ)	Incident-photon-to-current-conversion-efficiency
J_{sc}	Short circuit current density
k	Kinetic rate constant
k_B	Boltzmann constant
L	Length
L_D	Electron diffusion length
LHE(λ)	Light harvesting efficiency
Li-TFSI	lithium bistrifluoromethylsulfonyl imide
LUMO	Lowest unoccupied molecular orbital
MeCN	Acetonitrile
n	Electron concentration
NHE	Normal hydrogen electrode
OPV	Organic photovoltaic
p	Hole concentration
P	Power density
R_{ct}	The charge transfer resistance of electrons over the TiO_2/electrolyte interface
R_{FTO}	The charge transfer resistance of electrons over the FTO/electrolyte interface
R_{Pt}	The charge transfer resistance of between the electrolyte and counter electrode interface
R_S	Serial resistance
R_t	The electron transport resistance
SEM	Scanning electron microscopy
spiro-OMeTAD	2,2',7,7',-tetrakis(N,N-di-p-methoxyphenyl-amine)-9,9',-spirofluorene
U_{photo}	Photo-voltage
V_{oc}	Open-circuit voltage
T	Temperature
tBP	4-*tert*-butylpyridine
T_g	Glass transition temperature
ToF	Time-of-Flight
TPA	Triphenylamine
ZnPc	Zinc phthalocyanine
W	Watt
$Z^{'/''}$	Real/Imaginary impedance
Z_{diff}	Impedance from electrolyte diffusion

$\varepsilon(\lambda)$	Extinction coefficient
η	Energy conversion efficiency
λ	Wavelength in nanometer
μ	Charge mobility
σ	Ambipolar conductivity
τ_n	Effective electron lifetime
τ_{rec}	Electron recombination lifetime
τ_{trans}	Electron transport time
Φ_{Coll}	Quantum efficiency of electron collection
Φ_{Inj}	Quantum efficiency of photo-excited electron injection
Φ_{Reg}	Quantum efficiency of photo-oxidized dye regeneration

1. Introduction

1.1 Motivation

Our demand for energy has never been higher; it fuels not only our cars and airplanes but also our everyday life. While it is often said that the prosperity of a country could be gauged from how much energy an average person uses every year it also tells us something about the future. During 2005, an average Swedish person consumed roughly 5.8 tonnes of oil equivalent (toe) of energy per year, while the world average was merely 1.8 toe.[1] As the developing world is striving for the same standard of living as the developed world an increase in our future demand for energy can be expected. The sources from which our electrical energy stems are broadly divided into two categories, renewable and non-renewable. The non-renewable category contains fossil fuels such as coal, oil and natural gas but also fissile radioactive materials such as uranium or thorium. In 2009 non-renewable fuel sources accounted for as much as 80.5 % of our total electrical energy demand, see Figure 1. The global electricity consumption exceeded $1.9 \cdot 10^4$ TWh.[1]

A combination of increasing energy demands and global warming as a consequence of the combustion of fossil fuels has increased the driving force for researching and installing power production from renewable sources.[2] Hydropower has long been the only major renewable electrical energy source but other contenders are entering the race. Among these are the rapidly growing field of wind power (198 GW), photovoltaic (40 GW), geothermal power (11 GW) and ocean power (0.5 GW) with the 2009 estimation of global installed capacity shown in the round brackets.[3]

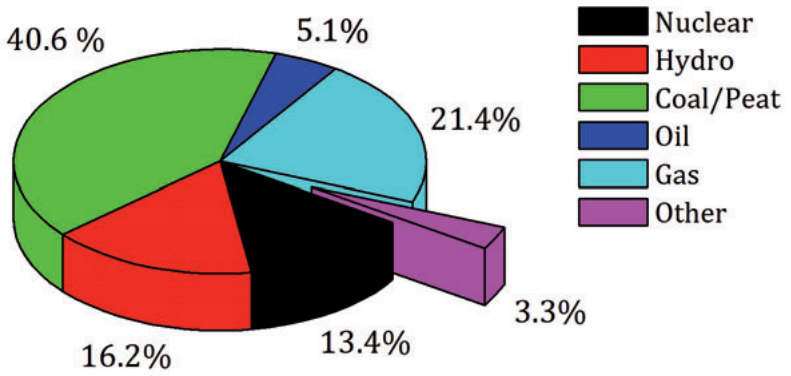


Figure 1: Total world electricity generation by fuel in 2009. The total amount of electricity generation was $2.0 \cdot 10^4$ TWh. The category *'other'* includes electricity generation by geothermal, solar, wind and heat power together with combustible renewables and waste.[1]

1.2 Energy from the sun

To visualize the enormous potential of harvesting solar energy it is instructive to compare the sun's electromagnetic energy reaching the surface of Earth to our electrical energy needs. Roughly 3-6 kWh of solar energy reaches the sea level per day and square meter, and if were to fill only $(350\ \text{km})^2$ with solar cells with efficiencies of 10 %, we could generate $2 \cdot 10^4$ TWh of electricity yearly. [4]

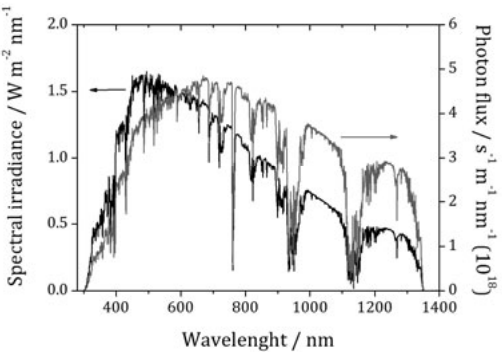


Figure 2: The standard solar spectral irradiance distribution (left y-axis) and the corresponding solar photon flux distribution (right y-axis).[5]

But for photovoltaic (PV) applications, it is not only the total energy of the sun's radiation that is important but also the spectral composition of the light. The PV important part of the solar spectrum can be divided up into the ultra-violet, visible and near infra-red regions where the UV-visible (280-

750 nm) and the near infra-red (750-1200 nm) regions combined contain roughly 84 % of the energy and 67 % of the photons [a]. Figure 2 shows the standardized terrestrial solar spectral irradiance distribution at an absolute airmass (AM) of 1.5, defined as 1000 W m^{-2} together with the corresponding solar photon flux distribution.[5]

1.3 Overview of the photovoltaic concepts

1.3.1 History of inorganic solar cells

The photovoltaic effect was discovered by Edmond Becquerel, a French physicist, in 1839 but it would take more than a hundred years before solar cells were actually used outside the laboratory for the generation of electricity.[6] It was the knowledge gained from the transistor research field, a field dominated by silicon, which sparked renewed interest in photovoltaic applications. Semiconductor technology developed after the Second World War by AT&T Bell laboratories were successfully transformed into working solar panels which could supply a useful amount of electrical energy.[7] Due to the initial low performance and prohibitive costs, the research field lay dormant for decades, only being kept on life-support by the space industry. A short revival during the oil crisis of the 70's renewed the commercial and public interest in photovoltaics, but the price was still not sufficiently low for the industry to gain pace. Since then, the solar cell industry has relied on computer chip manufacturers for a cheap supply of the high purity grade silicon needed to make highly efficient solar cells. Currently, inorganic solar cell efficiencies range from 30 % for multi-junction gallium arsenic solar cells to 20-25 % for crystalline silicon and thin film CIGS ($CuInGaSe_2$) to 17 % for cadmium telluride.[8] All these inorganic solar cells have one thing in common: they are sensitive to material impurities, a draw-back which adds significant costs to acquiring materials and producing these types of solar cells.[9]

1.3.2 Organic photovoltaics

A rather new research field has during the last couple of years rapidly gained momentum: photovoltaics based on organic semiconductors and hybrid systems. The main goal of these technologies are not to produce higher efficiency than solar cells based on inorganic semiconductors, but rather to produce the electricity cheaper by keeping production costs low. Solar cells based purely on organic semiconductors offers the exciting possibility of fast roll-to-roll manufacturing on flexible substrates, opening up the possibility of not only covering flat surfaces with solar cells, but also structured objects. Or-

[a] Calculated from the total power between 280-4000 nm.

ganic semiconductors for solar cell applications have broadly taken two directions; solution-processed light-absorbing semiconducting polymers or evaporated small molecular pigments and semiconductors.[10]

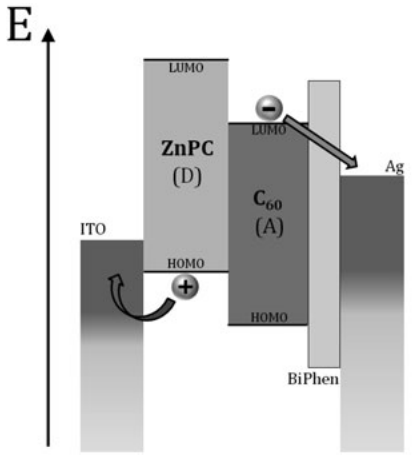


Figure 3: A schematic diagram of a planar heterojunction solar cell based on a light absorbing donor material (ZnPC) and an electron accepting material (C_{60}), sandwiched between two metal contacts. If the donor-acceptor interface is mixed it is called a bulk heterojunction solar cell.

Although the operating principles of organic solar cells are somewhat similar to inorganic ones, they are not as well understood. The main difference in operation between inorganic and organic solar cells is the dissociation of the photo-excited state, the exciton. The exciton is the bound electron-hole pair, which in inorganic semiconductor has low binding energies while the binding energy for organic material can be substantial.[11] Figure 3 shows the operating principle of an organic photovoltaic (OPV). It consists of a light absorbing electron donating (D) material in which the exciton is formed by photon absorption. To form a charge separated state, the exciton has to move to a dissociation site, often formed on the D-A (acceptor) interface. If the driving force is sufficiently large to overcome the binding energy of the electron-hole pair it can dissociate into free charge carriers. If this criterion is not met the exciton recombines and the energy of the absorbed photon is dissipated.[10]

One of the key challenges to optimize an OPV device is the balance between absorbing enough photons in a sufficiently thick absorbing layer while reducing the distance excitons and free charge carriers have to travel before being dissociated or collected. One of the more efficient approaches to maximize this property is to create a mixture of the D-A material, so to increase the light absorbing material volume while keeping the distance between the formed exciton and the D-A interface short.[12] The OPV used in this thesis

was ZnPC (a donor material) co-evaporated with the fullerene C_{60} (an electron accepting material) to form a bulk heterojunction (BHJ) solar cell, the device geometry can be seen in Figure 3.

1.3.3 Photoelectrochemical cells

An electrochemical solar cell based on a meso-porous wide band gap metal oxide sensitized with a dye exhibiting an efficiency of 7 % was demonstrated by Brian O'Regan and Michael Grätzel in 1991.[13] Since then the efficiency has increased to above 12 % and a significant research effort is under way to improve this type of solar cell further.[14-23] The electrochemical solar cell or the dye-sensitized solar cell (DSC) is built using cheap and abundant materials such as titanium dioxide (TiO_2), a wide band gap n-type semiconductor which is not only non-toxic but also chemically stable. The light absorbing material in the DSC is a sensitizer dye which is often anchored on the TiO_2 material through carboxylic groups. A liquid electrolyte based on the iodide/triiodide (I^- /I_3^-) redox couple is used to shuttle electrons from the counter electrode to the photo-oxidized sensitizer dye. All components are schematically shown in Figure 4, and the preparation method of DSC material and the assembly of the solar cells can be found in chapter 4. The DSC can be described as a device controlled by several competing electron transfer (ET) processes, each with their own rate constant.[24] According to Marcus theory the rate of electron transfer reactions depend on the electronic coupling and the free energy difference between the transfer states.[25]

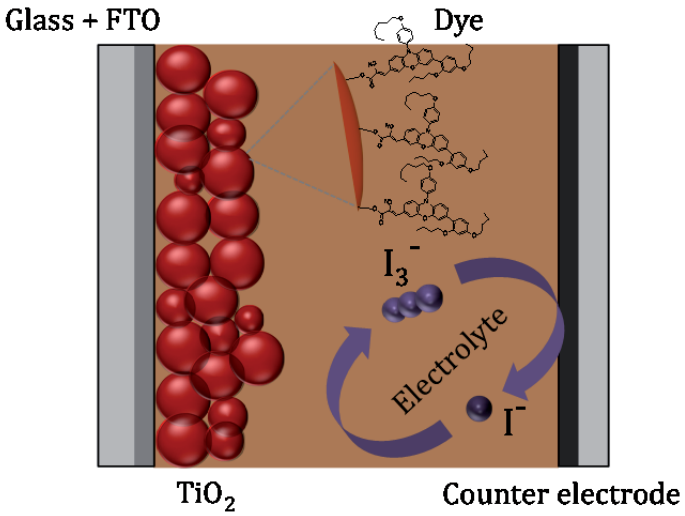


Figure 4: A schematic drawing of the dye-sensitized solar cell.

One of the main merits of the DSC over other organic photovoltaic technologies is that the photo-excited state is formed at the interface where the

charge separation takes place, eliminating the need for an exciton diffusion step. But since this charge separation interface is only a single molecule layer thick there has to be a very large surface area to ensure that most photons are being harvested by the sensitizer dye.

It was this limitation which was overcome, by O'Regan and Grätzel in 1991, by introducing a meso-porous network of TiO_2 particles, effectively increasing the surface area by several orders of magnitude.[13] The redox electrolyte system for highly efficient solar cells is regularly based on the volatile solvent acetonitrile (MeCN). As MeCN has a low boiling point of 81.2 °C, solvent evaporation is one of the major reasons for solar cell efficiency degradation after extended periods of operation.[26] Additionally, the highest photo-potentials achievable with the I^-/I_3^- redox couple is limited by large losses in over-potential in the dye regenerations step. These problems have stimulated an exploration of solid organic semiconductors to substitute the liquid electrolyte in DSC. In 1998 there was a breakthrough by Bach *et al*. using a new p-type organic semiconductor 2,2',7,7',-tetrakis(N,N-di-p-methoxyphenyl-amine)-9,9',-spirofluorene (spiro-OMeTAD), see Figure 5.[27]

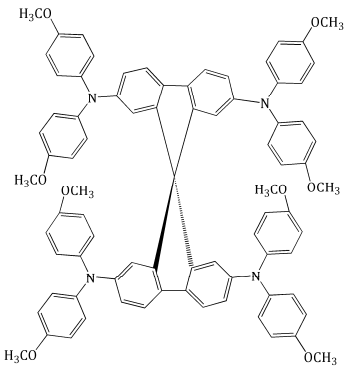


Figure 5: The small p-type organic semiconductor 2,2',7,7',-tetrakis(N,N-di-p-methoxyphenyl-amine)-9,9',-spirofluorene.

Naturally this type of solar cell device came to be called solid-state dye-sensitized solar cell and the efficiency has since increased from the initial 0.74% to more than 7%.[28-29] The lower efficiency obtained for the solid-state DSC device compared to their liquid electrolyte counterpart is believed to originate from the higher electron recombination as well as an insufficient penetration of the solid hole transporting material (HTM) into the meso-porous network of TiO_2.[28] This has effectively limited the TiO_2 electrode thickness which can be used for preparing these devices, and thus the light harvesting capabilities of these solar cells.

1.5 Aim of the thesis

The aim of this doctorial thesis is to characterize and to increase the understanding of solid-state dye-sensitized solar cells by identifying problems and limitations to the current state-of-the-art DSC device. Equally important is to investigate new strategies and methods to circumvent these device limitations and through that improve the performance of solid-state DSC devices. The following chapters are written as an introduction of previous work done within the field of dye-sensitized solar cells. Since the field in its entity is too large to cover in a single doctorial thesis the selection of references should be seen in the context of the scientific work presented below.

The following chapters of this thesis will be outlined below: Chapter 2 describes the materials used in both the liquid electrolyte and solid-state DSC. Chapter 3 contains a thorough discussion about the general operating principals behind the DSC as well as an examination of known problems associated with DSC. Chapter 4 describes common methods for the characterization of complete solar cells and of the materials used for making both the liquid and solid-state DSC. In total six papers are included into this thesis. Each paper is summarized in chapter 5 where the most important findings are presented to the reader. Chapter 6 contains the concluding remarks of this thesis work, where it started, where it went and in my opinion where it should go in the future. The last parts of this doctorial thesis contain, as customary, a Swedish summary, acknowledgement and references.

2. Materials for the dye-sensitized solar cells

This chapter discusses the similarities and differences between dye-sensitized solar cells using liquid electrolyte and solid-state hole transporting materials. Both solar cell types are made up of four main components: A working electrode made from a semiconducting metal oxide, a light absorbing material, a hole transporting medium and a counter electrode. Each of these components is critical for the solar cell device performance and will be described in the following subsections.

2.1 The working electrode

The working electrode material of dye-sensitized solar cells are deposited on transparent conductive oxide (TCO) coated glass substrates. Fluorine doped tin dioxide (FTO) is a commercially available TCO substrate which has a high thermal stability, a low sheet resistance (8 Ohm/sq.) and a low haze, properties which makes it the substrate of choice in DSC manufacturing. The electrode material itself is usually an intrinsic n-type semiconductor such as TiO_2, tin dioxide (SnO_2), tungsten trioxide (WO_3) or zinc oxide (ZnO).[30] These metal oxides are normally made from a sol-gel process route yielding size tuneable nano-particles. TiO_2 with anatase crystal structure, the most commonly used metal oxide for DSC, has an indirect band gap transition at 3.2 eV with a conduction band potential of colloidal particles at E_{cb} (TiO_2) = -0.12 – 0.059(pH) V vs. NHE.[31-32] In Figure 6b it is possible to see individual TiO_2 nano-particles as prepared by a sol-gel method and imaged with scanning electron microscopy, the particle size is around 15-20 nm in diameter. The anatase structure is not the only possible phase structure present in sol-gel prepared colloidal films, there may also be the thermodynamically stable rutile phase and some small amounts of brookite.[33]

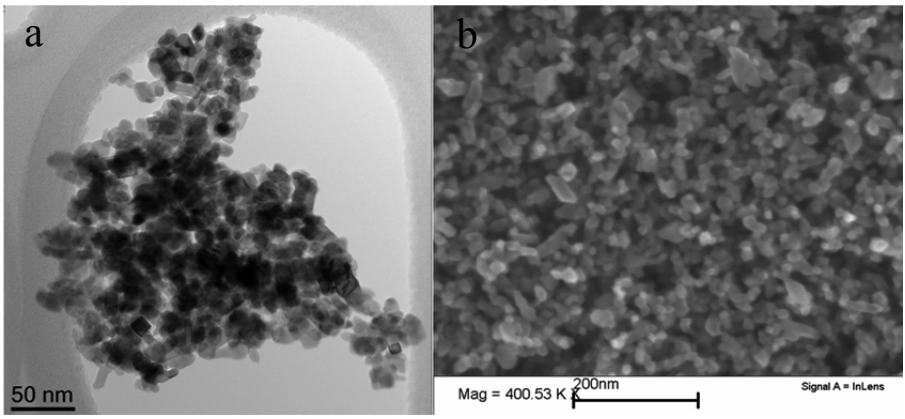


Figure 6: A transmission electron microscopy image of SnO_2 particles prepared by a sol-gel method (a, left). A scanning electron microscopy image of a sintered TiO_2 film prepared from a colloidal paste of TiO_2 nano-particles (b, right).

To form a high surface area scaffold of meso-porous TiO_2, necessary for building efficient DSCs, the nano-particles are dispersed in a viscous paste which then can be doctor-bladed[b] or screen-printed to form films of thicknesses up to 20-30 micrometer (μm). TiO_2 films formed in this manner need to be heated up, sintered, to temperatures between 400 and 500 °C. This sintering step ensure that all additives of the paste (solvent, binders and pore-forming agents) decompose and evaporate and that the individual TiO_2 particles fuse together, forming an electronically active meso-porous network.[34]

One of the most important parameters of the meso-porous network is the surface area. This can be measured using the BET gas adsorption technique[c] and from that deriving a roughness factor.[35] For meso-porous films with TiO_2 particles made from a sol-gel route the roughness factor routinely reaches values of 1000, meaning that the real area or inner surface area of a sintered TiO_2 film is 1000 times larger than the geometric area.[14]

2.1.1 TiO_2 blocking layers made by spray pyrolysis

One inherent property of a meso-porous network is that it does not completely coat the entire FTO substrate and thus leaves exposed FTO surfaces in contact with the electrolyte. For liquid electrolyte DSC based on the I_3^-/I^- redox couple the exchange current at this interface is negligible at short circuit conditions but significant at applied potentials.[37] This increase in dark current when applying a potential is even more pronounced for solar cell

[b] Doctorblading is a technique for spreading a solution across a surface using a spacer to control the final thickness of the film.
[c] BET = Brunauer, Emmett and Teller, after the inventors describing the technique.[36]

devices which use a solid-state hole transporting materials and an unprotected FTO/HTM interface. The material of choice for building solid-state DSC has long been spiro-OMeTAD. Spiro-OMeTAD acts like a current conductor in the solar cell and if there is a direct contact between the metal like FTO substrate and spiro-OMeTAD, large dark currents densities will run through this junction at applied potentials and lower the conversion efficiency of the solar cell.[37] Forming dense, pin-hole free, TiO_2 blocking layer is therefore very important for the efficiency of the solid-state DSC.[27,38-39] The most common method of creating these TiO_2 blocking layers is through spray pyrolysis.[27]

The spray pyrolysis method relies on spraying a solution containing the precursor of interest onto a hot surface. The droplets from the aerosol either reach the hot surface or turn to gaseous precursors which then react with the substrate due to elevated temperatures.[40] TiO_2 blocking layers for solid-state DSC are often made by spraying a solution of titanium(IV)acetylacetonate onto the hot (450 °C) FTO substrate surface.[38] The meso-porous TiO_2 film is then deposited on top of the dense blocking layer, so as to create a rectifying junction between the spiro-OMeTAD and the FTO substrate.

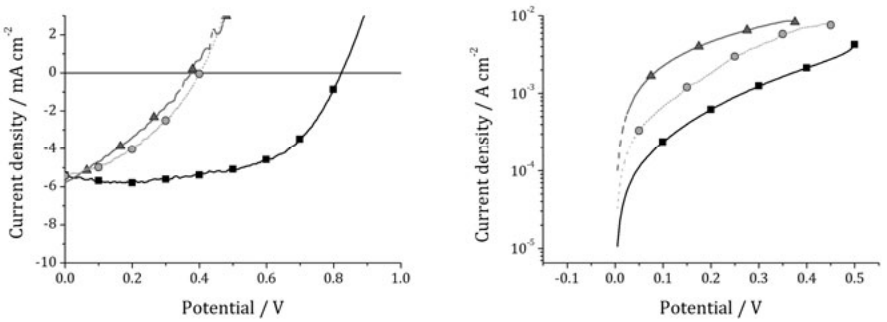


Figure 7: Solid-state DSC devices based on D102 and spiro-OMeTAD with no blocking layer (triangles), with a blocking layer made by a $TiCl_4$ treatment (circle) and blocking layers with 4 cycles of spray pyrolysis (square). Devices were measured at 1000 W m^{-2} in the left figure and in darkness in the right figure.

In Figure 7 it is possible to see the effect on the conversion efficiency of solid-state DSC devices where the blocking layers have been prepared in different ways. The dark grey curve with triangles in Figure 7 represents the J-V curve, in the light and the dark, for a solid-state DSC with no blocking layers. The light grey circles and black squares in the J-V curve represent blocking layers which were either prepared by $TiCl_4$ treatment of the FTO substrate or by 4 cycles of spray pyrolysis, respectively. Solar cell devices made with blocking layers which were poorly rectifying yielded low per-

forming solid-state DSC devices partly because they have larger dark current densities running through the FTO/HTM junction at applied potentials.

2.2 The light absorbing material

The most important part of the DSC is the light absorbing component. There are broadly three different categories of light absorbers for DSC: Metal-organic complexes, all organic dyes and quantum dots.[28,41-42] Figure 8 shows the dye structures of the record holders in two first classes based on the highest reported efficiency in solid-state DSC. The record holder using quantum dots in solid-state DSC are made with PbS.[42]

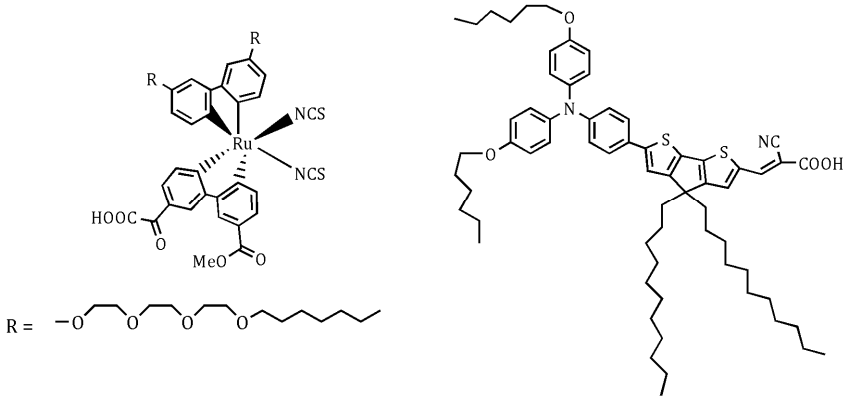


Figure 8: On the right panel the organic molecular structure of the sensitizing dye, C220,[28] for solid-state DSC is shown and on the left panel the record holder for ruthenium complexes for solid-state DSC, K68.[41]

Organic dyes have reached higher efficiencies, in solid-state DSC, than metal-organic complexes based on Ruthenium (Ru). The main reason for this is that organic dye molecules regularly have higher extinction coefficients ($\varepsilon(\lambda)$) compared to metal-organic complexes. Z907, the most commonly employed Ru-complex, has a maximum extinction coefficient of $12.2 \cdot 10^3$ $M^{-1}cm^{-1}$ while for example the organic dye, D102, has a 4-fold higher extinction coefficient of $55.8 \cdot 10^3$ $M^{-1}cm^{-1}$.[43-44]

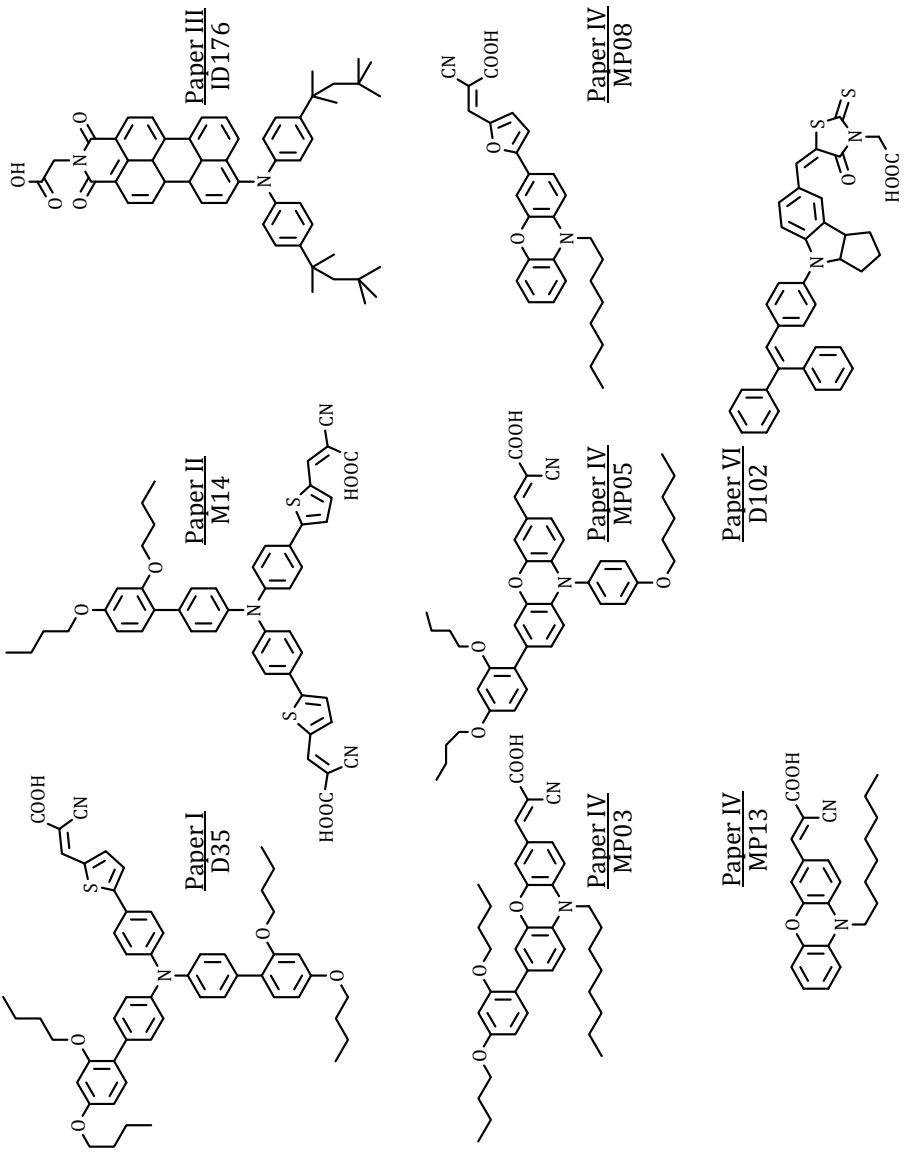


Figure 9: The molecular structures of sensitizing dyes used during this thesis and the first paper they are used in: D35 (*Paper I*), M14 (*Paper II*), ID176 (*Paper III*), MP03-MP13 (*Paper IV*), D102 (*Paper VI*).

The molecular structure of D102 can be seen in Figure 9 together with the molecular structure of all other sensitizers used in this thesis. Figure 9 also contains the reference to the paper in which the molecule is used.

Beyond the need for the dye to absorb photons they also have to transfer the photo-excited electrons from the dye molecule to the TiO_2. The proximity between the dye and the TiO_2 surface is controlled though the carboxcylic anchoring group on the dye molecule. In the simplest form, the anchoring group forms chelating bond between the hydroxyl group of the TiO_2 surface with the carboxylic group of the dye.[45-46] But proximity alone does not suffice for photo-excited electron injection to occur. The energy level of the excited state has also to be sufficiently high to allow for electron injection. Organic molecules have energy levels, in analogy with the valance and conduction band of inorganic semiconductors, which are called the highest occupied molecular orbital (HOMO) and lowest unoccupied molecular orbital (LUMO), respectively. These values are approximately related to the electrochemical oxidation and reduction potentials which are given in Table 1 as oxidation potentials ($E^{\circ\prime}_{(D^+/D)}$) and reduction potentials ($E^{\circ\prime}_{(D/D^-)}$), determined by electrochemistry for a dye in solution. It is advisable to avoid making direct comparisons of data in Table 1 since electrochemical data might be sensitive to small differences in experimental conditions.

Table 1. Absorption and electrochemical characterization of dyes

Dye Name	$\varepsilon(\lambda)$ / M^{-1} cm^{-1} (10^3)	Abs_{max} / nm	$E^{ox}_{(D+/D)}$ / V vs. NHE	$E^{red}_{(D/D-)}$[a] / V vs. NHE	Ref
D35	31	471	1.04	-1.1	*Paper I*
M14	50	504	1.07	-1.1	*Paper II*
ID176	25	575	1.21 (film)	-0.6 (film)	*Paper III*
D102	56	488	1.1[b]	Not reported	Ref: 47
MP03	40	480	0.88	-1.3	*Paper IV*
MP05	35	453	0.90	-1.3	*Paper IV*
MP08	37	493	1.0	-1.3	*Paper IV*
MP13	34	470	0.87	-1.3	*Paper IV*

[a] : Estimated from the 0-0 energy transition, the intercept of the normalized absorption and emission spectra in EtOH.
[b] : Measured against a Hg/Hg_2, KCl(sat) reference electrode, shifted to the NHE scale by 0.24 V.[48]

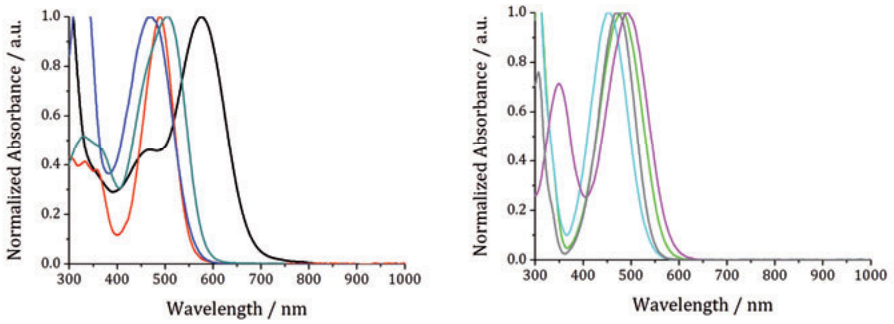


Figure 10: Normalized absorption spectra of the 8 dyes used for this thesis. Measured in EtOH solution and labelled from left to right: D35 (Blue), D102 (Red), M14 (Dark green), ID176 (Black), MP05 (Cyan), MP13 (Grey), MP03 (Green), MP08 (Magenta).

To evaluate how many photons are converted into electrons in DSC it is interesting to determine the light harvesting efficiency (LHE) of a device, which can be derived from the absorbance, *Abs,* of the dyed TiO_2 film.

$$LHE(\lambda) = 1 - 10^{-Abs(\lambda)} \qquad \text{Eq. 1}$$

The LHE(λ) of a film is determined by the amount of dye attached to the oxide surface which depends on the thickness and porosity of the mesoporous TiO_2 film. The LHE(λ) is also determined by the extinction coefficient of the dye and the width of the absorption peak. Ruthenium dyes, for example, often have a wider absorption peak, but a lower overall extinction coefficient, than organic dyes.

2.3 Electrolyte/Hole transporting material

The function of the redox electrolyte, or the hole transporting material, in the DSC is to shuttle electrons from the counter electrode to the photo-oxidized dye molecule. A liquid electrolyte of I^-/I_3^-, or cobalt-complexes, are to date the most efficient electrolyte systems in DSC.[13,22,49-50] Redox electrolytes are ionic conductors in which charges are transported via diffusion (concentration controlled) or by migration (electric field controlled). In the DSC the ionic conduction mainly takes place by diffusion, a process which occurs because the reduction-oxidation cycles at each electrode deplete and replenish the redox active species at each interface. Other types of liquid electrolytes have successfully been tried in the DSC configuration such as ferrocence and disulfide/thiolate.[51-52]

Holes are not a physical entity but rather a description of an electron vacancy in a system. A hole transporting material transfer charges by electronic conduction rather than through ionic mass transfer. Spiro-OMeTAD has so far proven to be the best hole transporting material used in the solid-state DSC configuration but there are other types of materials too.[27,53-54] Inorganic materials such as CuSCN and CuI have both proven to work efficiently as well as organic oligomers/polymers based on the thiophene and vinylene cores.[55-61] Small organic molecules have been investigated to a smaller extent including molecules with triphenylamine (TPA) moieties for which the molecular structures are seen in Figure 11.[21,62]

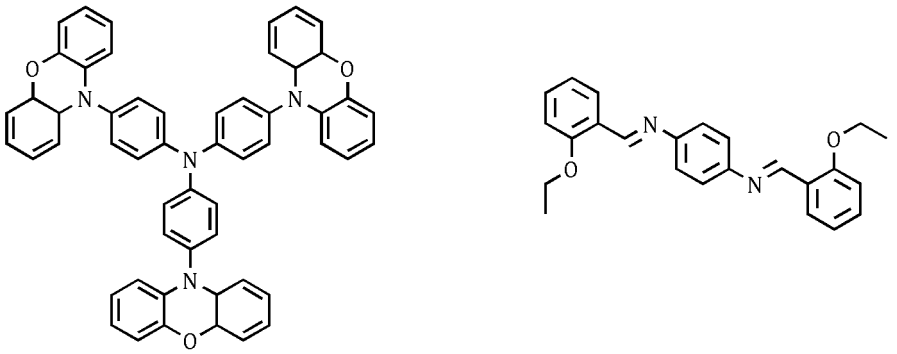


Figure 11: Molecular structures of hole transporting materials for solid-state DSC: HTM 4 (left) and HC3 (right).[63]

Spiro-OMeTAD belongs to a class of materials called amorphous molecular glasses, which in their solid-state glass phase, are characterized by a disorder in molecular distance and orientation as well as being in a thermodynamically non-equilibrium.[64-65] The stability of the molecular glass state is determined by the molecular structure and it is often referred to as the glass-transition temperature (T_g), the temperature where the amorphous glass state changes from being a solid brittle material to having a malleable elastic texture. The T_g was improved to 120 °C in the spiro-OMeTAD molecule from the parent fluorene moiety by the inclusion of the spiro-centre.[27,66-67] Another important feature of spiro-OMeTAD is its better solubility, since it is applied on the solar cells from a solution in organic solvents. Spiro-OMeTAD is soluble to roughly 200 mg/mL in chloro-benzene as well as in other chlorinated solvents, tetrahydrofuran and acetone. The solubility of spiro-OMeTAD together with the wetting properties of these solvents on TiO_2 have shown, so far, that chloro-benzene yields the most efficient solar cells.

2.4 Solar cell additives

Additives are usually molecules or materials which have been found to increase the DSC device performance when added to any step of the solar cell manufacturing process. Efficient additives are often found through screening of molecules and/or by extensive optimization of DSC devices. One of the most important additives or surface modification is the $TiCl_4$-treatment of the TiO_2 meso-porous working electrode, a treatment which improves device performance in liquid electrolyte solar cells and is crucial for efficient solid-state DSC devices.[39] The effect of $TiCl_4$-treatment depends on the quality of the particles used for making the meso-porous TiO_2 electrode but has in most cases been found to increase the short-circuit photo-current by reducing the interfacial electron-hole recombination.[68-69] Another important additive which is used both in liquid electrolyte and solid-state DSC is 4-*tert*-butylpyridine (tBP), see Figure 12.

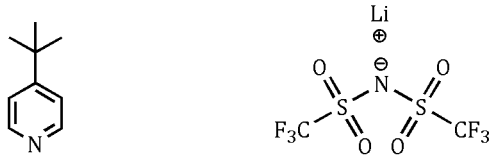


Figure 12: Molecular structure of solar cell additives 4-*tert*-butylpyridine (tBP) to the left and the Li-salt, lithium bistrifluoromethylsulfonyl imide (Li-TFSI), to the right.

tBP is a volatile molecule which is usually added to the liquid electrolyte in a concentration of around 0.5 M. The tBP molecule can coordinate to the TiO_2 surface by physiosorption through the electron donating nitrogen.[70] In the DSC it is believed that this coordination will shift the TiO_2 conduction band potential (E_{cb}) negatively by displacing ions, such as Li ions and protons, on the TiO_2 surface as well as reducing electron-hole recombination by restricting electrolyte access to the TiO_2 surface.[71] In the solid-state DSC the effect of the addition of tBP to the spiro-OMeTAD has been less studied. It does play a role in increasing the TiO_2 E_{cb} as well as reducing the doping density in DSC device made with spiro-OMeTAD.[72] In *Paper V* it was also shown that the tBP influences the solubility of the lithium bistrifluoromethylsulfonyl imide (Li-TFSI) salt in the solid spiro-OMeTAD matrix.

The Li-TFSI salt is known to shift the TiO_2 E_{cb} positively when used as an additive in the liquid electrolyte DSC.[73] The same effect occurs for the solid-state DSC but for this type of solar cell the Li-TFSI salt is an absolute necessity for obtaining a working solar cell.[17] The reason for this is still unknown but it has been suggested that Li ions screen columbic fields which develop between the charge separated state of the TiO_2 and the dye.[74-76] It has also

been suggested that the Li ions increase the charge mobility in the organic hole transporting medium by opening up a new pathway which channels holes through the organic semiconductor.[77] The Li-salt has been believed to be a redox inactive molecule towards spiro-OMeTAD but Figure 13 shows how a solution of spiro-OMeTAD, dissolved in Cl-benzene with and without Li-TFS,I oxidizes with time when stored under light. The increase in absorption at 520 nm corresponds to the 1st oxidation peak of spiro-OMeTAD, see Figure 18 for the complete absorption spectra of both ground state and oxidized spiro-OMeTAD. The oxidation process is slow in the presence of Li-TFSI but absent when there are no Li-TFSI molecules in the solution.

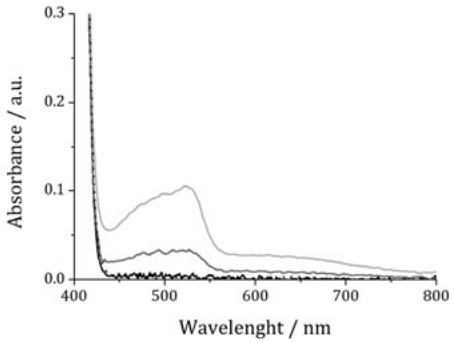


Figure 13: UV-VIS of the oxidized spiro-OMeTAD in a solution of Cl-benzene with and without Li-TFSI. The absorption seen at 520 nm corresponds to the 1st oxidation peak of spiro-OMeTAD, and is increasing with storing time under light condition and Li-TFSI. Storage time of the sample containing Li-TFSI is 1 day (black), 4 days (dark grey) and 18 days (light grey) while the sample without Li-TFSI is stored for 18 days and is shown as the black dotted curve at the baseline.

Paper V further explores the oxidation behaviour of spiro-OMeTAD in presence of Li-TFSI and the implication this effect might have on the operation of solid-state DSC devices. There are many other additives used in the DSC which will not be further explained in this thesis. For example deoxycholic acid derivatives are sometimes used to split up dye aggregates in the dye bath solution, during the sensitization of the TiO_2 electrode, an effect which has shown to increase the device performance.[78-79] It is also possible to treat the meso-porous TiO_2 network with various acidic additives, such as phosphonic acids, which has shown to chemisorb onto the TiO_2 surface and to increase DSC device performance.[80-81]

2.5 Counter electrode

The counter electrode is responsible for completing the internal electrical circuit by injecting electrons back into the electrolyte. In the liquid electro-

lyte DSC based on the I^-/I_3^- system the counter electrode is built on a TCO substrate on which a platinum (Pt) electrocatalyst is deposited by thermal means from a solution of an organoplatinum compound.[13,82] Others types of electrocatalyst have been proven to work efficiently such as carbon, CoS or NbO but have not yet gained wide spread use.[83-85] The most important parameter for an efficient electrocatalyst is the rate of reduction of the redox mediator, for example the reduction of I_3^-. This influences the performance of the DSC, where a low catalytic activity or a high over-potential add serial resistances to the solar cell.[49]

In solid-state DSC the counter electrode materials most commonly used are, thermally evaporated metals of silver or gold. Evaporation of reflective metal contacts has been recognized to increase the short circuit current density (J_{sc}) in solar cells by reflecting transmitted light back into the solar cell and thus increase the LHE(λ).[41] This is an important improvement since light capture in the thin TiO_2 electrodes used for solid-state DSC has so far limited the total conversion efficiency of these devices. There is very little known about the influence of the counter electrode material on the device operation of the solid-state DSC. There are some discussions about V_2O_5/Al contacts and Ag/Au contacts but very little on others.[41,86]

3. The operation of the dye-sensitized solar cells

The operational principle of the photoelectrochemical solar cells is based on several interfacial electron transfer and bulk charge carriers transport processes. A photon is absorbed by the sensitizing dye which promotes an electron from a lower energetic state to a higher energetic state, the system has absorbed energy. The photo-excited electron, which is also the carrier of the absorbed energy, is injected into the meso-porous network of TiO_2. The electron vacancy, or the hole, left on the dye molecule is reduced by I^- molecules from the electrolyte. The driving force for this regenerative electron transfer step is the more negative redox potential of the I^- with respect to the oxidized dye molecule. The injected electrons are transported through the meso-porous TiO_2 network by a diffusion process until they reach the FTO substrate where they can be collected by the external circuit. The oxidized I^- molecule on the other hand is going through several intermediate chemical transitions which finally forms the I_3^- molecule. This species diffuses in the electrolyte phase, until it reaches the platinized counter electrode, where it is reduced back to I^-.

This straight and simplified picture of the operation of the photoelectrochemical solar cell will serve well for a continued discussion about the origin of the photo-current and photo-voltage seen in these types of devices. Figure 14 shows the linear flow of photo-current in an idealized liquid electrolyte DSC.

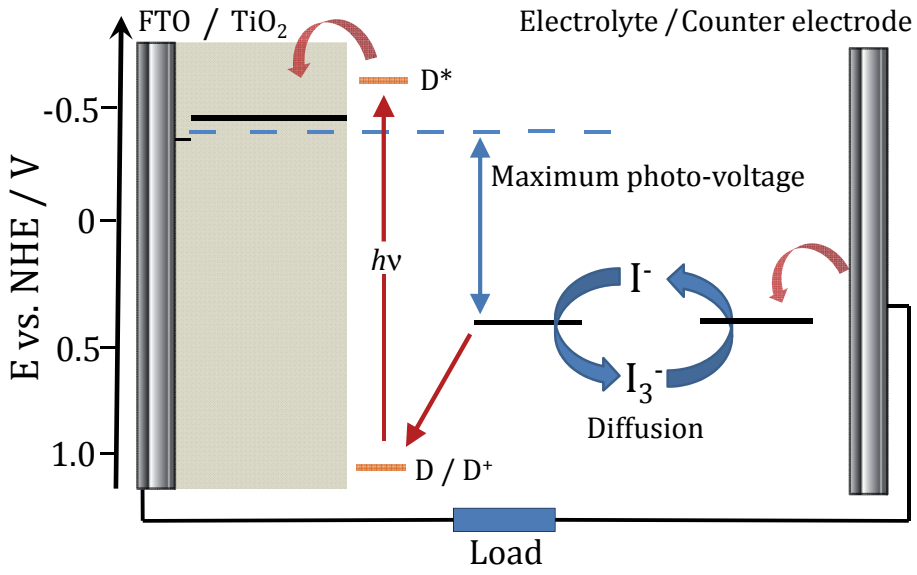


Figure 14: A schematic representation of how the photo-generated charges flow inside a liquid electrolyte DSC and how they are collected in the external circuit.

To understand the photo-voltage of a liquid electrolyte DSC it is first important to take a step back and look at the system in darkness as well as under different external loads, see Figure 15. In darkness and thermal equilibrium the TiO_2 electron Fermi energy ($E_{F,n}$) is equal to the redox energy of electrolyte ($E_{F,redox}$),[23,87] where the $E_{F,redox}$ is given by:[19]

$$E_{F,redox} = E^{\circ\prime}_{F,redox} - k_B T \, ln \frac{[I_3^-]}{[I^-]} \qquad \text{Eq. 2}$$

Eq. 2 represents the Nernst equation, written in the energy scale, where $E^{\circ\prime}_{F,redox}$ is the formal redox energy of the electrolyte, k_B is the Boltzmann constant and T represents the temperature. Under illumination the DSC system is perturbed by injected photo-electrons from the sensitizer dye to the TiO_2. The equilibrium $E_{F,n}$ is split under illumination into the quasi-Fermi energy levels ($E^*_{F,n}$) of electrons in the TiO_2 and $E_{F,redox}$ for the electrolyte.[88] The photo-voltage (U_{photo}) of the solar cell is related to the difference in energy level positions and is given by:

$$U_{photo} = \frac{E^*_{F,n} - E_{F,redox}}{e} \qquad \text{Eq. 3}$$

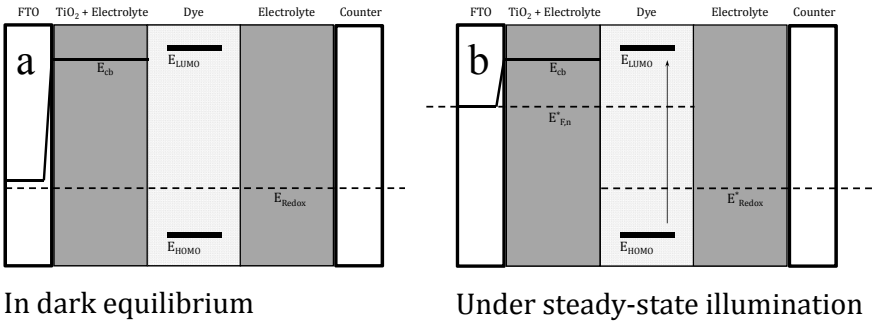
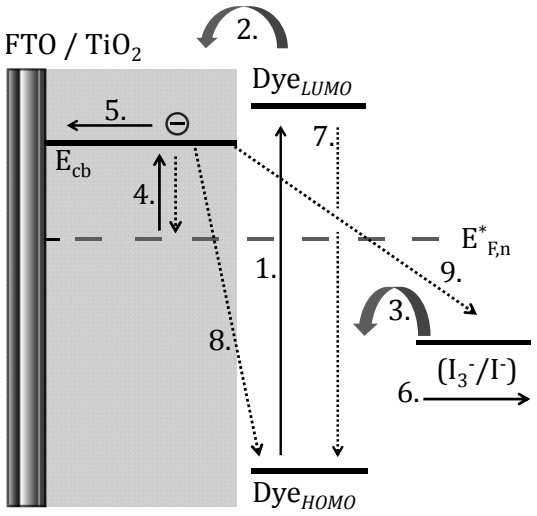


Figure 15: The formation of photo-voltage in a liquid electrolyte DSC when going from a state of thermal equilibrium in darkness (a, left) to a steady-state where the solar cell is illuminated and under an external load (b, right).

As the external load increases, so does the photo-voltage until the $E^*_{F,n}$ in the TiO_2 is equal to the TiO_2 E_{cb}. This is the ideal theoretical open-circuit potential (V_{oc}) of DSC where no back flow of current exists.[88] The real liquid electrolyte DSC does indeed have these back flow pathways where charges are flowing in the opposite direction, or as they are generally called recombination currents.

There are three main loss mechanisms in the DSC where photo-current is lost due to recombination currents: losses due to the relaxation of the photo-excited dye molecule, losses due to the photo-oxidized dye recapturing an electron from the TiO_2 and losses occurring when electrons in the TiO_2 recombine with the oxidized electrolyte species (the I_3^-). In Figure 16 all of the above-mentioned electron transfer processes are indicated, where black arrows indicate forward electron processes (good for the operation of the solar cell) and where red arrows indicate recombination currents, which are bad for the operation of the solar cell.



1. Photo-excitation
2. Electron injection
3. Dye regeneration
4. e^- trapping/ detrapping in TiO_2
5. e^- diffusion in TiO_2
6. Ionic diffusion of electrolyte
7. Relaxation of photo-excited state
8. e^- back reaction
9. e^- recombination

Figure 16: A schematic view over all electron transfer processes in a dye-sensitized solar cell based on a liquid electrolyte. Power generating steps are marked as solid lines while steps limiting the performance of the liquid DSC are marked in dotted lines.

The process in which electromagnetic energy is converted to a flow of electrons in the dye-sensitized solar could be described as several electron transfer steps, in which each step could be described by a kinetic rate constant. In the DSC several of these kinetic processes are in competition with each other. Some are positive for the operation of the solar cell, such as electron injection and dye regeneration, while some of them are negative, such as electron recombination and fluorescence.

It is the differences in kinetic rate constants which permits that an electrochemical potential can be built up between the TiO_2 phase and the electrolyte phase during illumination of the DSC device.[87] Without these differences the DSC would not be able to sustain any photo-potential and thus the DSC would not be able to convert any electromagnetic energy to electrical power. As will be shown below, the greater the differences, the higher the probability of charge carriers being transported and collected in the external circuit both with and without a load resistance. The most important steps were summarized above for a typical DSC device based on the I^-/I_3^- electrolyte, the corresponding reactions are also indicated in Figure 16.

3.1 Electron transfer steps in dye-sensitized solar cells

The measured rate constants associated with the reactions in Figure 16 are different for every system. To exemplify the range of rate constants (or time constants) for a system it is helpful to look at the most investigated system to date i.e. ruthenium sensitizer complexes on colloidal anatase TiO_2. In this system electron injection from the photo-excited state into the TiO_2 takes place in the femtosecond (10^{-15} s) to picosecond (10^{-12} s) range while electron back reaction and recombination happen on the millisecond time scale (10^{-3} s).[20,49,89-94] The rate constants for the electron diffusion in the TiO_2, electron back reaction and recombination are dependent on the light intensity. The reason and implication of this behavior is explained later. The reduction of the photo-oxidized dye happens on the microsecond (10^{-6} s) time scale.[93-95] Generally, for efficient DSC, forward reactions marked in black solid line in Figure 16 need to have larger rate constants than the corresponding competing reaction, marked with grey dotted lines. These relationships are commonly expressed in a simpler form where each process can be described as an efficiency. For example the electron injection efficiency (Φ_{Inj}) is written as a ratio of the competing kinetic processes, see equation 4.

$$\Phi_{Inj} = \frac{k_{inj}}{(k_{inj}+k_{rel})} \qquad \text{Eq. 4}$$

where k_{inj} is the rate constant for the photo-excited electron to be injected from the dye into the TiO_2 and where the k_{rel} is the total rate constant for the relaxation of the photo-excited state. From equation 4 it is apparent that a higher rate constant for electron injection is advantageous for the DSC device operation as well as having low rate constants for the relaxation. The same procedure can be applied for the dye regeneration (Φ_{Reg}) and the charge collection (Φ_{Coll}), see Eqs. 5 and 6.

$$\Phi_{Reg} = \frac{k_{reg}}{(k_{reg}+k_{back})} \qquad \text{Eq. 5}$$

$$\Phi_{Coll} = \frac{k_{trans}}{(k_{trans}+k_{rec})} \qquad \text{Eq. 6}$$

where k_{reg} , k_{back}, k_{trans} and k_{rec} are the rate constants for regeneration, back reaction, transport and recombination.

3.1.1 Diffusion processes

Both the transport of redox species in the electrolyte and electrons in the meso-porous TiO_2 network are diffusion controlled. First, the transport of electrons in the TiO_2 by diffusion is the result of a concentration gradient of electrons in the TiO_2 network. An electron concentration gradient can also be

viewed as a gradient in electrochemical potentials across the TiO_2 film. The gradient in electron concentration is the result of short-circuiting the solar cell under illumination and extracting charges from one of the contacts. This operation of DSC differs from that of regular *p-n* junctions in one important aspect, the abscence of an internal electric field. In DSC the drift current is often neglected since it is believed that there is a very small electrical field inside small intrinsically doped TiO_2 particles.[96] The correctness of this assumption is debated as well as the reason for having a light intensity dependent diffusion transport in meso-porous TiO_2.[14,97] Currently, the best model which describes the transport of electrons in the conduction band of TiO_2 is through a series of electron trapping and de-trapping events, in which the electron diffusion coefficient depends on the total amount of charge carriers in the film.[98-99]

When characterizing DSC it is common to ascribe the movement of electrons in the TiO_2 with a diffusion coefficient (D) and the time electrons are residing in the TiO_2 with a lifetime coefficient (τ). In analogy with the Φ_{Coll}, Eq. 6, a diffusion length (L_D) is calculated to describe how far an average electron can diffuse inside a meso-porous TiO_2 electrode before recombining.[97] The $\frac{\partial n_c}{\partial n_t}$ and $\frac{\partial n_t}{\partial n_c}$ terms in Eqs. 7 and 8 describe, the dynamic equilibrium between trapped electrons (n_t) and conduction band electrons (n_c).[100] The effective electron diffusion coefficient (D_n) is proportional to the concentration of electrons in the TiO_2 and the effective electron lifetime (τ_n) is inversely proportional to the concentration of electrons in the TiO_2. Eqs. 7 and 8 show the quasi-static approximation of the diffusion coefficient for free electrons (D_0) and the electron lifetime for free electrons (τ_0).[100]

$$D_n = (1 + \frac{\partial n_c}{\partial n_t})D_0 \qquad \text{Eq. 7}$$

$$\tau_n = (1 + \frac{\partial n_t}{\partial n_c})\tau_0 \qquad \text{Eq. 8}$$

$$L_D = \sqrt{D_n \tau_n} \qquad \text{Eq. 9}$$

The diffusion length is the average displacement of electrons associated with D_n and τ_n, and where the dependence of n_c and n_t is effectively canceled out when determining the L_D.[99-103] For efficient charge collection of electrons generated in the meso-porous TiO_2 network the L_D needs to exceed the film thickness.

The second diffusion process in the DSC is that of the redox mediator (I^-/I_3^-). The redox mediator forms an ionic circuit between the platinized counter electrode, where I_3^- is reduced to I^-, and between the TiO_2/dye interface, where I^- is oxidized to I_3^-. The molecular diffusion is driven by a concentration gradient build up by the regeneration of the photo-oxidized sensitizing

dye molecule. The absolute diffusion coefficient of ionic species varies with the viscosity of the solvent in which they are dissolved. For example the diffusion coefficient for I_3^- in MeCN is > $8.5 \cdot 10^{-6}$ cm^2s^{-1} while in the higher viscosity solvent 1-hexyl-3-methyl-imidazolium iodine it has a diffusion coefficient of $9 \cdot 10^{-8}$ cm^2s^{-1}.[104] The diffusion coefficient of redox species is not only determined by solvent viscosity but also on the size of the molecule. These as well as the concentration of the redox species influence the over-potential of the counter electrode and the maximum current density it can sustain.

3.2 Charge transfer processes in solid-state DSC

The solid-state dye-sensitized solar cell has very similar charge transfer steps as its liquid electrolyte counterpart. The main difference is that the charge transfer in solid-state DSC occurs through the HOMO level of the solid hole transporting material by a hopping mechanism rather than by ionic diffusion.[53,67,105-107] The hopping mechanism is the description of charge carrier transport through a disordered landscape of spatial and energetic states.[108-109] The charge transport in these materials can be of either electron or hole transporting character or they can have an ambipolar transport meaning that they conduct both electrons and holes. Spiro-OMeTAD, the most common material in this thesis, is only used as a hole transporting material.[53] Figure 17 shows a schematic picture of hole transport in a Gaussian distribution of energetic HOMO states, where holes are transported from the oxidized dye molecule to the counter electrode.

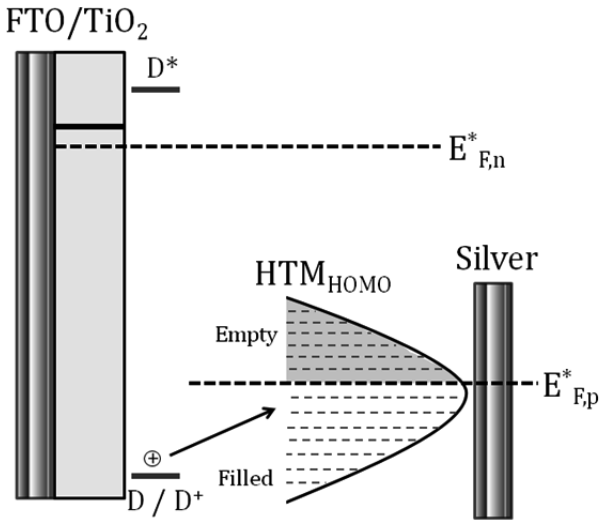


Figure 17: A schematic picture of the carrier transport in a solid-state molecular hole transporting glass using an ensemble of HOMO states which could be active in the charge transport of holes.

The ambipolar conductivity (σ) of a material can be written as a function of the mobility (μ) and the concentration of charge carriers, where holes are denoted as *p* and electrons as *n*, see Eq. 10. An efficient hole transporting material used for solid-state DSC application should be able to sustain current densities of more than 20 mA cm^{-2} in order for it not to be diffusion limited. For spiro-OMeTAD the electron conductivity is neglected, since it is assumed to be a hole transporter. Two studies of the mobility of spiro-OMeTAD have been published with values of $2 \cdot 10^{-4}$ $cm^2V^{-1}s^{-1}$ at $2.6 \cdot 10^5$ Vcm^{-1} and one with $1.4 \cdot 10^{-5}$ $cm^2V^{-1}s^{-1}$ at $1.2 \cdot 10^4$ cmV^{-1}. [53,77] These values are higher than those measured in time-of-flight measurements of *Paper V*, $1.0 \cdot 10^{-5}$ $cm^2V^{-1}s^{-1}$ at $2.5 \cdot 10^5$ Vcm^{-1}.

$$\sigma = e\, p\, \mu_p + e\, n\, \mu_n \qquad \text{Eq .10}$$

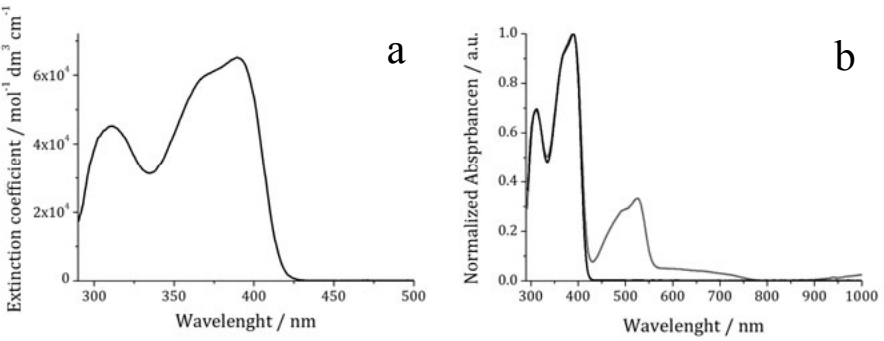


Figure 18: The extinction coefficient of spiro-OMeTAD in Cl-benzene (a, left) and the absorption spectra of both oxidized and non-oxidized spiro-OMeTAD in Cl-benzene (b, right).

The charge carrier concentration in a semiconducting material can be either intrinsic or extrinsic in nature, intrinsic charge carrier comes from the temperature dependent Fermi-Dirac distribution while extrinsic charge carrier can be introduced in the material by photo-doping, impurities or chemical doping. The doping density of spiro-OMeTAD can be detected by absorption spectroscopy by the absorption of the extra vacant state the doping introduces in the HOMO level. Figure 18a shows the extinction coefficient of spiro-OMeTAD in a Cl-benzene solution and Figure 18b shows the absorption spectrum of oxidized spiro-OMeTAD in the same solvent. Note especially the oxidized peak at 520 nm with a long extended tail towards 800 nm. An additional oxidation peak starts rising at 900 nm. This very broad absorption of the oxidized species of spiro-OMeTAD together with its large extinction coefficient of $3.3 \cdot 10^4$ $M^{-1}cm^{-1}$ at 507 nm complicates the interpretation of how much light is absorbed by the dye and how much is absorbed by the HTM.[110] What is clear is that an absorption peak of the oxidized spiro-OMeTAD stretching over much of the visible spectra will result in a significant filtering effect, reducing the photo-current generated by the sensitizing dye.

The photo-doping effect, which involves the increase of charge carriers within the spiro-OMeTAD due to injection of holes from the photo-oxidized dye can be seen in Figure 19. This photo-doping effect was measured using a three electrode setup with two silver electrodes, used for measuring the resistivity, evaporated on top of a solid-state DSC. The short-circuit current was varied by changing the illumination power yielding very similar results as previously report by Snaith *et al.*[111]

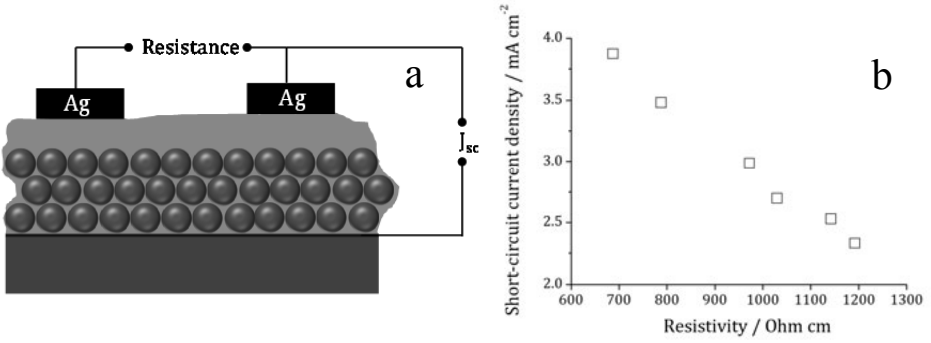


Figure 19: A schematic view of a three electrode solid-state DSC containing two evaporated silver contacts used for measuring the resistivity of spiro-OMeTAD in a working device (a, left). An increase in short-circuit current density, or number of injected holes in the spiro-OMeTAD, corresponds to a reduction of the resistivity in spiro-OMeTAD, according to Eq. 10 (b, right).

In its pure state spiro-OMeTAD is almost an insulator with very low conductivity, the doping density and its conductivity can easily be modified by chemical doping, as seen in subchapter 4.2.3 where spiro-OMeTAD is doped with Li-TFSI. When the solid-state DSC was introduced it was very common to add a chemical dopant, often an antimony complex, to the spiro-OMeTAD matrix.[27,39,112] Since then the use of chemical dopants in solid-state DSC have fallen out of practice. Recently, however, a very efficient solid-state DSC device was demonstrated built with a cobalt complex as dopant. This device currently holds the record of 7.2 %.[29]

The solid-state DSC has an even faster reduction rate of the photo-oxidized dye than the liquid electrolyte DSC. The hole transfer rate from a ruthenium dye (N719) to spiro-OMeTAD has been measured to occur on a time scale between 3 ps and 1 ns with 50 % of the dye being reduced after 900 ps.[105] Because of this much faster regeneration rate compared to liquid DSC the dye regeneration in solid-state DSC is often assumed to be close to unity.[113]

3.3 Obstacles for increasing conversion efficiency in dye-sensitized solar cells

In liquid electrolyte DSC the existing limitations for increasing the device efficiency are twofold. The first one regards the insufficient light harvesting in the near-infrared region for the sensitizers to date used in DSC. There exists near-infrared dyes which absorb light to higher wavelengths but these dyes are usually limited in conversion efficiency, mainly due to the low output photo-voltage these devices are yielding. The optimal band gap for a

sensitizer dye follows that of the Shockley-Queisser limit, which determines the theoretical optimum band gap of a single absorbing material to 1.1 electronvolt (eV).[114] This theoretical limit predicts a maximum conversion efficiency just above 30% for a perfect absorber in an ideal solar cell. The dye-sensitized solar cell has electronic losses which cannot be neglected in this analysis and will influence the optimum band gap energy of the sensitizing dye. Some of these losses are necessary for driving electron transport processes in the solar cell while others are over-potential losses which can be avoided in an optimized DSC device. By comparing the absorption onset for the dyes in Figure 20, which ranges from 575 nm to 700 nm (equals 2.16 eV - 1.77 eV), with the theoretical limit of 1.1 eV it is possible to see that large amount of photons which could be harvested for electricity generation never are absorbed by the dye at all.

The second drawback of the liquid electrolyte DSC based on I^-/I_3^-, which is limiting its conversion efficiency, is the large losses from over-potential in electron transfer steps. Consider the standard ruthenium dye (N719) which has an absorption onset of 750 nm and an open-circuit potential of 0.85 V at 1000 Wm^{-2}.[115] Even for this very efficient DSC there is a loss-potential of ~0.80 V. This loss in potential has two main components; potential loss at the electron injection step from dye to TiO_2 ($\Delta V_{inj} = 0.25\,V$) and the over-potential in the reduction of the photo-oxidized dye ($\Delta V_{reg} = 0.6\,V$), see Figure 20.[116]

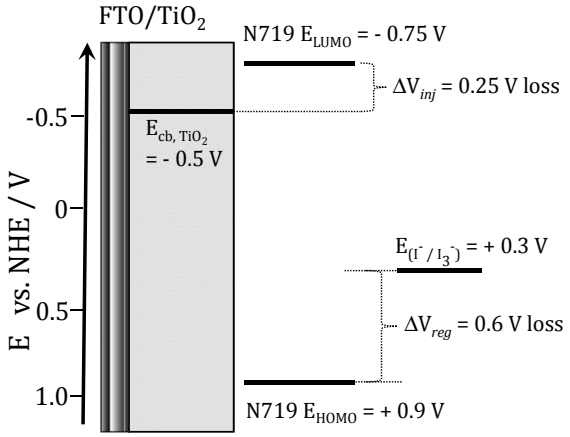


Figure 20: There are large potential losses in liquid electrolyte DSC based on the I^-/I_3^- electrolyte. The two main losses are from over-potentials in the dye regeneration and for electron injection.

It is this over-potential in the dye regeneration step for the I^-/I_3^- redox mediator which is one of the main motivator trying to find new redox mediators, both liquid electrolytes and solid-state HTM. Many of the new redox media-

tors which have been reported have a lower potential drop for the dye regeneration but also has a shorter electron lifetime, with implications for the current and photo-voltage of these devices.[51-52,117] The shorter electron lifetime for some liquid electrolyte redox mediators, others than that of the I^-/I_3^-, are attributed to the faster interfacial recombination kinetics of electrons in the conduction band of TiO_2 with oxidized redox species in the electrolyte. Empirically, this is a common observation, for one-electron, outer-sphere redox couples such as ferrocene and cobalt-complexes.

The same higher rate of electron recombination is also limiting the device efficiency for solid-state DSC based on spiro-OMeTAD.[110,118] Electron diffusion lengths for liquid electrolyte solar cells based on I^-/I_3^- have been reported with a wide spread of values, ranging between 80 µm,[103] 16 µm,[119] 20-100 µm,[118] 30-60 µm,[120] to 40-70 µm.[121] Thus, L_D is significantly longer than the actual TiO_2 thickness. The L_D for solid-state DSC on the other hand are significantly shorter with values of 4 um,[122] 2-20 µm,[111] 6-13 µm,[101] 2-6 µm,[123] 0.6-6 µm,[124] and 0.8-3 µm.[118] This shorter L_D in solid-state DSC reflects the shorter electron lifetime in these devices rather than different change transport dynamics of the TiO_2.[111] One other important difference can be discerned by comparing the L_D for liquid and solid-state DSCs. It is often found that the L_D changes with $E^*_{F,n}$ and in the liquid electrolyte DSC L_D is increasing with $E^*_{F,n}$ while the opposite is true for solar cells based on solid-state HTM.[101]

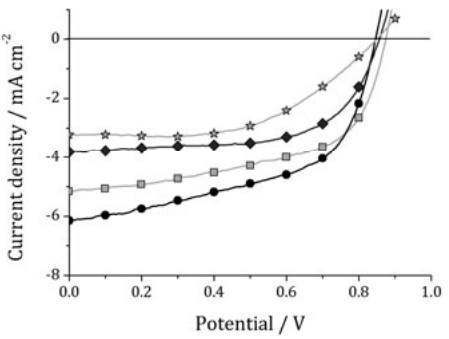


Figure 21: The impact of variations in working electrode thickness in solid-state DSC based on spiro-OMeTAD and the sensitizer, D102. Thicknesses: 3.15 µm (stars), 2.53 µm (diamonds), 1.46 µm (squares) and 1.88 µm (circles). All samples are measured at 1000 Wm^{-2} (AM1.5G).

Empirically, the optimum thickness of the meso-porous TiO_2 network for use in solid-state DSC based on spiro-OMeTAD has been determined to be around 2 µm. This thickness is not thick enough to absorb and convert enough photons to electricity to yield devices with efficiencies above 10 %. This constraint in device thickness is not well investigated but it is proposed

that the limitation arises from poor filling of the voids/pores of the meso-porous TiO_2 network with the organic semi-conductor.[39] This pore-filling effect has recently been investigated showing that a better performing solar cell device can be obtained when increasing the amount of spiro-OMeTAD inside the pores.[123,125-126] Figure 21 shows how relative small changes in thickness of the TiO_2 meso-porous network can influence the performance of solid-state DSC. The effects seen in the figure below does not only reflect a change in pore-filling but also changes in absorption of these devices (for example note the lower photo-current for the 1.46 μm device compared to the one of 1.88 μm) as well as changes in the thickness of the over-standing layer and charge collection efficiency.

3.4 Stability of dye-sensitized solar cells

For commercialization of the DSC it is not only important to have high solar energy conversion efficiency but also questions regarding production costs and stability needs to be addressed.[16] Stability issues are covered in the scientific literature to some extent with stability optimized electrolyte DSC being reported to retain > 95 % of the initial device efficiency for 1000 hr.[16,127] Both stable (1000 hr and 1 sun) and efficient (4.6 %) solid-state DSC based on organic dye molecules have been reported.[128] So far, device stability has been of lower priority than device efficiency. However, with increasing efforts for the industrial realization of DSC products stability becomes more important.

4. Methods

4.1 Solar cell preparation and assembly

The specific preparation methods to assemble DSC can be found in the experimental sections of each paper but some general practices will be presented in the subchapters below. The differences between dye-sensitized solar cells with a liquid electrolyte and a solid-state hole transporting material are few but significant and are therefore noted in the subchapters below. The preparation method of the bulk heterojunction solar cell device, which is one half of the tandem cell, differs on the other hand substantially from the preparation method of the DSC and is therefore given in a longer introduction in chapter 4.1.3.

4.1.1 Liquid electrolyte dye-sensitized solar cells

The preparation and assembly of the liquid electrolyte DSC is carried out in several consecutive steps, namely: the formation of the meso-porous TiO_2 working electrode, the coloration of the working electrode with the sensitizing dye, the infiltration of the liquid electrolyte and the sealing of the solar cell. The FTO substrate, on which the DSC solar cell is built on, is coated with a commercial TiO_2 paste (Dyesol, DSL 18NR-T) by screen printing,[23] doctor-blading,[34] spin coating.[129] The TiO_2 paste coated FTO substrate is then sintered, a process in which the substrate is treated through a slow heating program up to temperatures of 450 °C. This sintering process assures that all organic solvents, binders and fillers present in the TiO_2 paste burn away leaving only a meso-porous structure of the inter-connected TiO_2 particles behind.[130] To adsorb the sensitizing dye to the sintered TiO_2 structure the hot electrodes are submersed into a solution containing the dissolved dye. The dye solution penetrates the meso-porous TiO_2 network slowly and it is usually required to leave the working electrode for more than ten hours in the dye solution to assure dense enough packing of dye molecules on the TiO_2 surface to yield good working DSC devices.[130]

A similar heating step as above is applied when preparing the platinized counter electrode. The counter electrode is built on a FTO substrate where two pre-drilled holes will allow for the introduction of the electrolyte into the solar cell. The counter electrode is coated with an ethanol solution con-

taining a chloroplatinic acid compound, the subsequent sintering step decomposes the compound into metallic platinum, which will act as a catalyst for injecting electrons into the liquid electrolyte DSC by reducing the I_3^- species in the electrolyte.[130]

Having formed the basis of a dye-sensitized solar cell by attaching the dye molecules on the large surface area TiO_2 structure, the solar cell is assembled by melting the working electrode and the platinized counter electrode together using a thermoplastic foil. The thermoplastic foil is used to create a barrier for solvent evaporation between the two substrate glasses but also to form a lateral spacer between the working electrode and the counter electrode, to avoid short-circuiting the DSC device by forming a physical connection between the two.

The exact liquid electrolyte composition varies greatly but almost always includes iodine (I_2) and a source of iodide ions (I^-) dissolved in a solvent.[16] The electrolyte is introduced into the DSC solar cell through the hole in the counter electrode glass. The wetting of the internal space of the solar cell is facilitated by capillary forces between the substrate/TiO_2 and the solvent. To increase this wetting and remove gas bubbles trapped inside the meso-porous TiO_2 network it is common to subject the open solar cell to a low pressure step.[130] Finally, the liquid electrolyte DSC is completed by sealing the inlet holes in the counter electrode by melting a thermoplastic foil and a glass cover over the holes. This prevents further evaporation of solvent from the internal space of the solar cell.

4.1.2 Solid-state dye-sensitized solar cells

The preparation of solid-state DSC differs only slightly from that of the liquid electrolyte DSC. The main differences lie in the application of the hole transporting material as well as the need for a TiO_2 blocking layer. The latter is often a dense layer of TiO_2 which is deposited on the FTO electrode usually by spray pyrolysis which has been described in detail in section 2.1.1.[38,40,131]

The next big difference in the preparation method between liquid and solid-state DSC is the infiltration of the electrolyte and the solid-state hole transporting material, respectively. The liquid electrolyte can be introduced into the meso-porous network of the solar cell by capillary forces. The solid-state HTM on the other hand is dissolved in a volatile solvent, often chlorobenzene, and is spin coated into a solid film where the solvent is expected to evaporate quickly. In practise the dyed thin meso-porous TiO_2 working electrode, roughly around 2 μm, is placed on a rotating table on which the substrate is hold down by vacuum suction. By covering the TiO_2 working elec-

trode with dissolved HTM, often spiro-OMeTAD, it will penetrate into the structure by capillary forces. The penetration depth of the solid-state HTM is thought to depend both on the soaking time and the concentration of the solute but also on the viscosity of the dissolved solution.[125] The spin coating procedure is applied to remove excess solid-state HTM and to form a uniform layer of the HTM on top of the meso-porous TiO_2 network. This layer is usually referred to as the overstanding layer and is thought to be necessary to avoid a direct contact between the evaporated back contact and the TiO_2. The exact nature of this filling process in solid-state DSC is not well understood but it is believed to be the limiting step in increasing the device performance.[111,123,125]

Finally, the solid-state DSC device is completed by the evaporation of a back contact, commonly silver or gold. This contact is responsible for injecting electrons into the device from the external circuit. All the contacts used in this thesis have been applied on the solar cell by thermal resistive evaporation through heating of a tungsten filament by passing high currents through it until it is glowing hot.

4.1.3 A sDSC and bulk heterojunction tandem device

The tandem solar cell presented in *Paper VI* is a mixture of a solid-state DSC prepared as described above, but instead of using a thick reflective contact it has a thin (2 nm) transparent silver electron-hole recombination layer. On top of this solid-state DSC device is an inverted small molecule bulk heterojunction solar cell evaporated. Figure 22 shows the schematic device setup for a novel tandem solar cell which reaches efficiencies of 6 %. The evaporation of the organic BHJ solar cell is made by loading the complete first half cell, the solid-state DSC, into a vacuum chamber. The first evaporation step is the silver recombination layer followed by a 6 nm exciton-blocking layer of 4,7-diphenyl-1,10-phenanthroline (Biphen) and a 20 nm layer of C_{60}. After these 3 layers a 40 nm layer of zinc phthalocyanine (ZnPc) and C_{60} are co-evaporated to form an interpenetrated network responsible for the photo-activity of the BHJ solar cell. For a comprehensive description of the instrumentation and the functioning of this type of BHJ solar cell please refer to this excellent reference.[12]

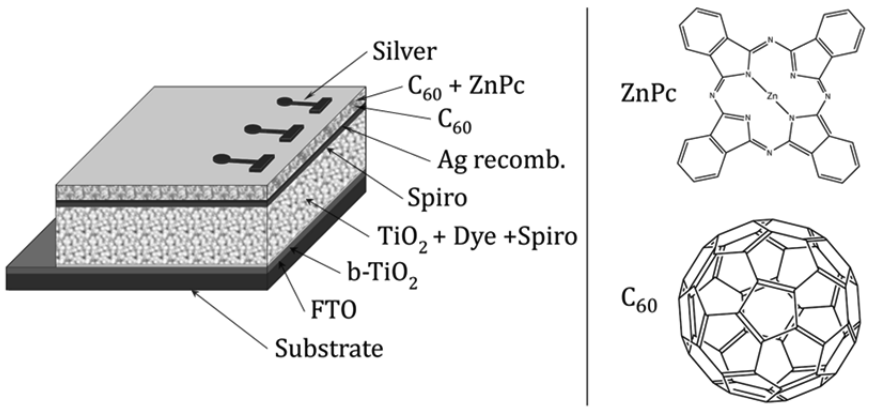


Figure 22: A schematic picture of the device setup used for a novel tandem solar cell based on solid-state DSC and the BHJ solar cell. The molecular structure of ZnPc and C_{60} can be seen on the right hand side of the figure.

4.2. Preparation of Materials for DSC

4.2.1 Colloidal metal oxide particles for DSC

The preparation of colloidal metal oxide particles is often made through the sol-gel route. With this method it is possible to obtain particle sizes which ranges from the low nanometer size to hundreds of micrometers from various metal oxides such as TiO_2, SnO_2, ZnO, ZrO, Ta_2O_5, WO_3, NiO and many others.[132-133] The metal oxide systems used in this thesis were either commercially available or synthesized in the laboratory according to previously developed routes. In *Paper I* the working material used was cassiterite SnO_2 with an average particle size of 8 nm. These particles were prepared by metal hydrolyzation/precipitation of $SnCl_4$ in basic conditions followed by a hydrothermal method to increase particle sizes. Investigations of product crystallinity and particle dimensions were carried out with X-ray diffraction techniques (XRD) and transmission electron spectroscopy.[134]

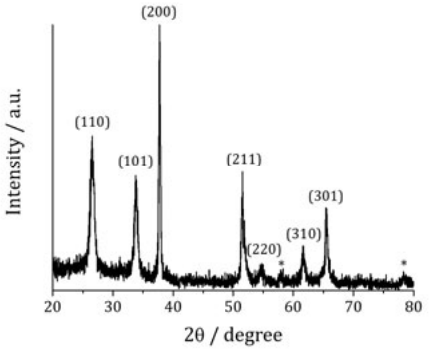


Figure 23: A powder X-ray diffractogram of calcinated (450 °C) SnO_2 particles synthesized as described above. The resulting diffractogram peaks had a high correlation with the cassiterite SnO_2 (JCPDS 21-1250) with the corresponding peak indicated in the figure. The diffractogram was recorded using a Siemens D5000 with Cu Kα radiation. The * indicate from left to right: (112) and (321).

The crystallinity of the prepared SnO_2 paste was measured with XRD, the resulting diffractogram is shown in Figure 23 with a very high correlation with the SnO_2 cassiterite phase. A commercial paste of colloidal TiO_2 particles (Dyesol, DSL 18NR-T) was chosen for *Papers II-VI*, mainly because optimized solar cells using this paste outperformed non-commercial, home-made pastes.

4.2.2 Core-shell structures by atomic layer deposition

There is no general agreement on what defines a core-shell structure and for the reader and the clarity of this thesis it will be defined as a system where one spherical core material is coated with an outer shell material. For DSC applications core-shell structures have been successfully utilized when the shell was deposited through both liquid and vapor phase methods.[135-137] The effect this type of surface modifications will have on a DSC device is not only dependent on which materials are chosen for the core-shell structure but it is also believed to be sensitive to both coating uniformity and to the coating method. Applying gas phase methods over liquid phase deposition techniques is believed yield to higher control over parameters such as coating thickness and conformity.

Atomic layer deposition (ALD) is a less common variant in the big family of vapour deposition techniques, developed to coat surfaces through gas phase reactions. This technique will not be thorough explained in this thesis but the following references will provide the interested reader with the basic background information.[138-139] These 5 steps cover the general ALD process when

coating a metal oxide on a high aspect-ratio surface, as used for creating the SnO_2-TiO_2 core-shell seen in *Paper I*:

- Formation of a reactive surface by removing adsorbed water molecules from the meso-porous SnO_2 surface by heating (300 °C) under an inert gas flow.

- Exposition of the reactive hydroxyl groups on the SnO_2 surface to a carrier gas containing the metal precursor, $TiCl_4$, invoking a chemical reaction between the $TiCl_4$ species and the tin dioxide surface.

- The reactor chamber is purged from all unreacted precursor molecules with an inert carrier gas as well as removing all volatile reaction products.

- Exposition of the titanium covered SnO_2 surface to water vapour at elevated temperature leading to hydrolyzation of all remaining [Ti-Cl] bonds to form TiO_2 on the surfaces.

- Repetition of step 1 through 4 (constituting one ALD cycle). Consecutive reaction occurs now with free hydroxyl groups on the TiO_2 surface.

The resulting surface coverage using this layer-by-layer ALD technique has shown to have an excellent uniformity and a linear coverage response to the number of ALD cycles is applied.[140-141] Even if the schematic picture above suggest that a single monolayer of atoms would be deposited for every ALD cycles it has been shown, for other systems, not to be the case. Rather, the deposition rate depends on reaction temperature used in the ALD chamber, type of precursor and the templating material. Common techniques used for investigating core-shell structures include X-ray photoelectron spectroscopy and electron microscopy. Figure 24a shows how XPS can be utilized to follow the change in chemical composition of the outer most layer of the SnO_2-TiO_2 core-shell structures when varying the number of TiO_2 ALD cycles. The increase in XPS signal ratio shows the attenuation of the $Sn^{3d5/2}$ peak as the SnO_2 core particle is covered with atomic layers of TiO_2. From these measurements it is possible to estimate the TiO_2 coating thickness using the probability of inelastic scattering and the dampening of the $Sn^{3d5/2}$ signal.[142] The XPS measurements presented in *Paper I* have been recorded at the end station of beam line KMC-1 at the synchrotron facility BESSY in Berlin, Germany.[143] Further experimental details can be found in the experimental section of *Paper I*.

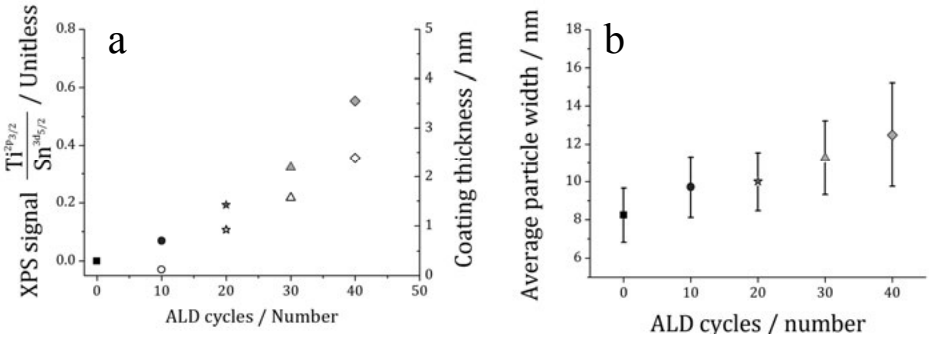


Figure 24: The change in chemical composition of the outer most layers of SnO_2-TiO_2 core-shell structures formed by atomic layer deposition and the estimation of coating thickness from XPS data (a, left). The average particle width of SnO_2-TiO_2 core-shell particles as measured from transmission electron spectroscopy pictures, each point represent at least an average of 40 particles (b, right).

Figure 24b shows how the core-shell particle increases in width when applying TiO_2 ALD cycles on the 8 nm SnO_2 core particle. Electron microscopy pictures were taken with a FEI Titan 300 transmission electron microscope (300 keV).

4.3 Characterization of complete solar cells

The are many techniques for characterizing solar cells, some are standard in the field such as current-voltage measurements (J-V) or incident-photo-to-current-conversion efficiency (IPCE), while others are less common. This section will broadly describe some measurement techniques used during this thesis but also refer the reader to appropriate and important references.

4.3.1 Current – Voltage (J-V) Measurement

For solar cells the single most important parameter is the efficiency of converting solar power into electrical power under illumination. This parameter is called conversion efficiency, usually just efficiency for short, and is defined as:

$$\eta = \frac{P_{out}}{P_{in}} \qquad \text{Eq. 11}$$

Where (P_{out}) is the amount of electrical power extracted from the solar cell divided by a known incident electromagnetic power (P_{in}). Both these physical quantities are generally expressed in the unit Watt ($J \cdot s^{-1}$) and the η is a unitless quantity expressed in percent.

While testing and comparing solar cells under a bright and cloud free summer sky would be the optimal testing conditions for solar cells, unfortunately these conditions rarely present themselves. In laboratory conditions one has to rely on artificial light sources such as filtered xenon or halogen lamps. With these light sources it is important to also know and trust the spectral distribution and the power of the light source used. For the characterization of solar cells light sources that simulate the spectral distribution and intensity of the standard solar spectrum are used, see Figure 2. Using standardized measuring conditions is important for publishing and comparing PV technology. The power of the light source is calibrated to resemble AM 1.5 G conditions (1000 Wm^{-2}) using a reference.

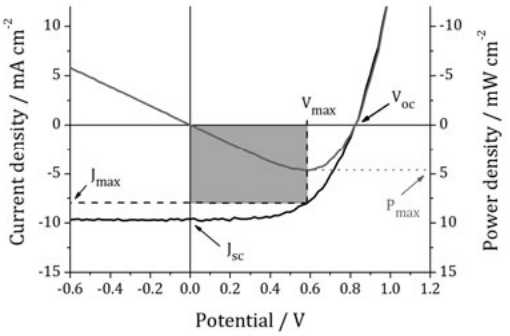


Figure 25: Power and J-V curve of a very efficient (4.8 %) solid-state DSC based on D102 and spiro-OMeTAD, prepared as explained in *Paper VI*. The figure marks all important solar cell parameters and where and how they are read out from the J-V curve; the shaded area represents the real power of the device (J_{max}·V_{max}) while the (J_{sc}·V_{oc}) represent the theoretical maximum of the device.

The P_{out} is the product of the measured potential and the flow of photocurrent from the solar cell under illumination. The point on the J-V curve which gives the highest power is called P_{max}, which has a corresponding V_{max} and J_{max}, as indicated in Figure 25. For comparing the performance between different solar cells it is customary to also indicate the photocurrent at zero applied potential, the short-circuit current density (J_{sc}) and the potential where no net current runs through the external circuit, the open circuit potential (V_{oc}), both indicated in Figure 25. It is also common to ascribe the solar cell a fill factor (FF) value which is defined through Eq. 12.

$$FF = \frac{J_{max}V_{max}}{I_{sc}V_{oc}} \qquad \text{Eq. 12}$$

The fill factor says something about the quality of the solar cell where a higher value means a better solar cell. The shaded area in Figure 25 repre-

sents the real power of the device ($J_{max} \cdot V_{max}$) while the ($J_{sc} \cdot V_{oc}$) represents the theoretical maximum of the device.

4.3.2 Incident-photon-to-current-conversion-efficiency

Incident-photon-to-current-conversion-efficiency (IPCE) is a measurement technique used to measure the spectral sensitivity of a solar cell. Instead of measuring conversion efficiency of a solar cell using a white light, IPCE is using a monochromatic light with a known flux. By scanning through each wavelength and simultaneously measuring the current output it is possible to measure the spectrally dependent photo-to-current conversion efficiency of a solar cell.

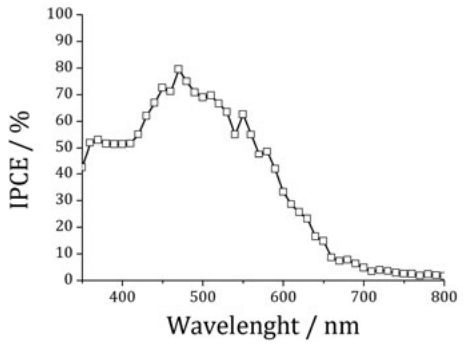


Figure 26: The incident-photon-to-current-conversion-efficiency of solid-state dye-sensitized solar cell based on the dye MP08, see *Paper IV*.

There are several different modes of operation for measuring IPCE, one technique is to measure the differential current caused by chopping a low irradiance monochromatic light on top of a white light pump. Another is to directly measure the photo-current of the monochromatic light without any background light. To measure IPCE of each individual subcells in a tandem solar cell configuration (see *Paper VI*) it is necessary to pump one subcell with a monochromatic light and then measure the spectral sensitivity of the other subcell, the current-limiting device, by scanning monochromatic light.

Figure 26 shows the spectral sensitivity of the MP08 dye in a solid-state DSC device based on spiro-OMeTAD. The maximum IPCE value is around 80 % with an IPCE onset at 650 nm, corresponding well to the absorption onset of the dye in solution (~600 nm). Now, having identified most of the important parameters for determining the device efficiency of a solar cell, it is possible to describe the IPCE as a function of the individual efficiency components as seen in Eq. 13. Because of reflectance and scattering losses of the glass/TCO/working electrode interface, the LHE(λ) seldom reaches

beyond 90% at the absorption maximum of dye. Thus, when reaching IPCE values of 80-90%, which is not uncommon in liquid electrolyte DSC, this is an indication of a near unity in efficiency of the individual components seen in Eq. 13.

$$IPCE(\lambda) = LHE(\lambda)\,\Phi_{Inj}\,\Phi_{Reg}\,\Phi_{Coll} \qquad \text{Eq. 13}$$

$$APCE(\lambda) = \frac{IPCE(\lambda)}{LHE(\lambda)} \qquad \text{Eq. 14}$$

It is sometimes useful to calculate the absorbed-photon-to-current-conversion-efficiency (APCE), Eq. 14 which then can be used to gauge if injection, regeneration or charge collection is a problem for a specific sensitizing dye. The integrated IPCE current also serves as an important cross-checking method to validate the short-circuit current density (J_{sc}) in the J-V measurement, see Eq. 15.

$$J_{SC} = e\int_{\lambda_{min}}^{\lambda_{max}} IPCE(\lambda)\,E(\lambda)d\lambda \qquad \text{Eq. 15}$$

where E(λ) is the photon flux of 1000 Wm^{-2} of an AM1.5 global solar spectrum as presented in Figure 2.

4.3.3 Electron lifetime measurements

In a solar cell it is important to know for how long an electron stay in a higher energetically state inside the meso-porous TiO_2 before returning to its equilibrium state. This time is usually called the electron lifetime and reflects the rate constant of one or several electron recombination processes taking place inside the solar cell. There are two main ways how these kinetic processes can be measured, either by intensity-modulated photo-voltage spectroscopy or by electrical impedance spectroscopy, see impedance section 4.3.6. Intensity-modulated photo-voltage measurements can either be performed with a sinus wave light modulation where the resulting voltage signal is resolved in the frequency space or as a small modulated square wave pulse where the resulting photo-voltage transient can be fitted with an exponential decay function, see Figure 27a and Eq. 16.

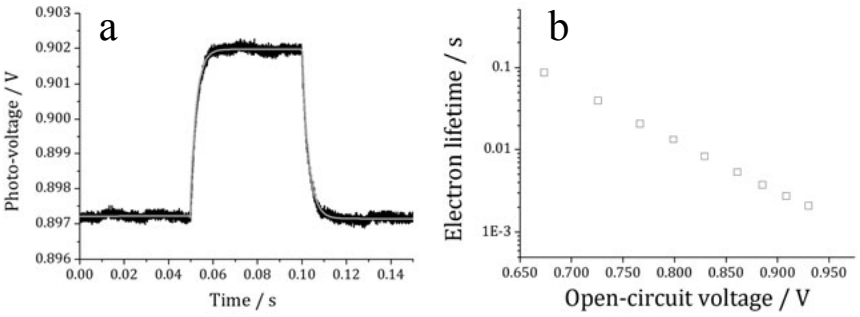


Figure 27: The transient photo-voltage of a solid-state DSC based on D35 under a small amplitude square wave modulated light (a, left). The black line is the measured data samples at 50 kHz and the grey line is the two part fitted data from Eq. 16. Fitted electron lifetime data measured for several orders of magnitude in light intensity as a function of open-circuit potential (b, right).

$$V_{oc} = V_0 \pm \Delta V_{mod}\, exp\left(^{-t}/_{\tau_{rec}}\right) \qquad \text{Eq. 16}$$

where V_0 is the photo-voltage offset, ΔV_{mod} is the photo-voltage difference from the small modulated light intensity, t is the time and τ_{rec} is the recombination lifetime of electrons. The ± sign before the right hand term in Eq. 16 describes if the function is a photo-voltage decay or growth. The recombination lifetime for a solid-state DSC device made on the dye D35 has been fitted to Eq. 16, seen as the light grey line in Figure 27a, and was determined to be $2.73(\pm 0.01)\cdot10^{-3}$ seconds at approximately 1000 Wm^{-2}. Using a single-exponential growth function, as Eq. 16, might not always be advisable when dealing with more complex recombination reactions but has yielded similar results as V_{oc} decay and IMPV measurements for small signal modulations.[144] The negative slope of the electron lifetime constant versus the open-circuit potential, as characteristically seen in DSC and in Figure 27b, is a consequence of the trapping-detrapping model describing electron transport in DSC. At higher open-circuit potentials the $E^*_{F,n}$ in the TiO_2 meso-porous network is higher and therefore the ratio of free-to-trapped electrons is also higher. A higher charge density of free electrons in the conduction band of TiO_2 increases the rate at which these electrons reach a recombination site from where they can recombine with holes in the electrolyte or HTM.

4.3.4 Electron transport measurements

Electron transport measurement can be performed using a similar approach as described in the previous chapter but instead of measuring the photo-voltage it is possible to measure the photo-current running through the external circuit of the solar cell. Square wave intensity-modulated photo-current

spectroscopy gives current transients with an exponential dependence on light intensity. The photo-current transient can be fitted with Eq. 17.

$$I_{sc} = I_0 \pm \Delta I_{mod}\, exp\left(^{-t}/_{\tau_{resp}}\right) \qquad \text{Eq. 17}$$

where I_0 is the photo-current offset, ΔI_{mod} is the photo-current difference from the small modulated light intensity, t is the time and τ_{resp} is the response time for electrons to be either extracted through the external circuit or re-combined with oxidized species in the electrolyte. Since the electron recombination lifetime could be independently determined, as described in the previous subchapter, it is possible to recalculate the electron transport time (τ_{trans}) from the electron response time through:

$$\frac{1}{\tau_{trans}} = \frac{1}{\tau_{resp}} - \frac{1}{\tau_{rec}} \qquad \text{Eq. 18}$$

Figure 28 shows both the electron lifetime and the electron transport in a solid-state DSC device based on dye D35 versus light intensity. It is important to note that these two curves are not measured under identical conditions; the electron lifetime (open symbols) is measured at open-circuit conditions with a high charge carrier density of electrons trapped inside the TiO_2 meso-porous network and where the charge density profile across the film is homogeneous. The transport time (filled symbols) is measured at short-circuit conditions with low charge carrier density and an inhomogeneous charge density profile across the film.[101]

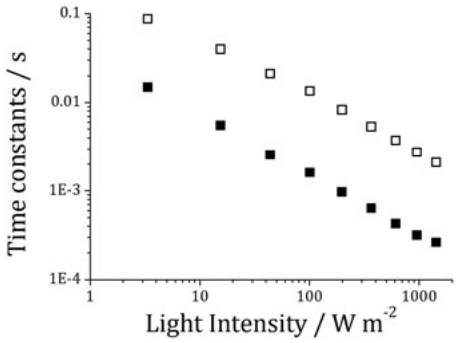


Figure 28: The fitted electron transport time (filled squares) and the electron lifetime time (open squares) versus light intensity from a white LED.

The parallel electron lifetime and transport time constants seen in Figure 28 supports the empirical observation that the light dependent electron trapping-detrapping mechanism for electron transport and recombination cancel out each other when determining the L_D, see Eqs. 7-9. An L_D determined from the data in Figure 28 would be an underestimation of the true L_D, because the

transport of electrons at the maximum power point (the most solar cell relevant point) would be faster than at short-circuit.[101]

4.3.5 Charge extraction techniques

Knowing the amount of charge carriers present in a DSC can be important when comparing different devices with each other. The amount of trapped charge is proportional to the $E^*_{F,n}$ and influences also the V_{OC}. One experiment to obtain the amount of charge carriers is to measure the open-circuit potential of a DSC device at a specific light intensity and then at the same time switch off the light and switch the device from the V_{oc} potential to short-circuit condition and measure the flowing current.[145] The integrated current density over a specific time corresponds to the amount of stored charges in the device minus the charges which has recombined during the charge collection time.

Seen in Figure 29 is the plot of open-circuit potential versus the integrated charge density of two liquid electrolyte DSC based on TiO_2 (filled squares) and SnO_2 (open squares) working electrodes. The lower V_{oc} seen in Figure 29 is a direct result of the lower conduction band edge of SnO_2 compared to TiO_2, relative to the redox mediator and the slope of the curve is a measurement of the trap density distribution of the meso-porous network of each material.[146]

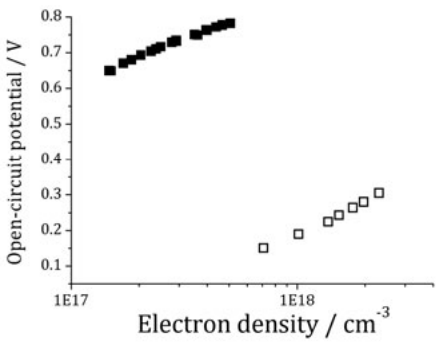


Figure 29: The open-circuit potential of a liquid electrolyte DSC device made with TiO_2 (filled squares) and with SnO_2 (open squares) as a function of extracted electron charge density in the material.

4.3.6 Impedance spectroscopy (EIS)

The fundamental understanding of electrical impedance of DSC has progressed significantly by work of for example Bisquert *et al*. and covers now both liquid electrolytes and solid-state hole transporting materials.[118,147-148] The most advantageous property of EIS is its possibility of resolving each

electron process in the operation of the DSC at every light and potential conditions. The biggest drawback of the technique is its large reliance on model building and how to assure that an accurate model are being used to fit actual measured data. Standard EIS uses sinus modulated voltage probe pulses and measures the resulting delayed/impeded current trace, resolved in the frequency domain, through the device under testing. Figure 30a shows the transmission line model developed by Bisquert *et al*. which is currently used to fit EIS data from liquid electrolyte DSC.[147]

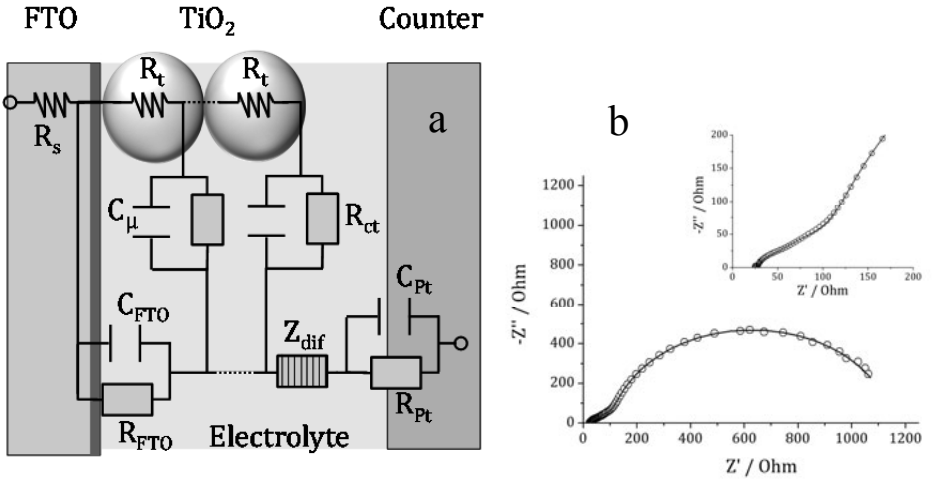


Figure 30: The transmission line model for liquid electrolyte DSC used for fitting EIS data, each separate element is described in the text (left, a). The impedance data was measured on a liquid electrolyte DSC made with MP05 and I^-/I_3^-, in light and at V_{oc}, data is shown as circles (right, b). The solid line represents the best fitting of impedance data and the inset shows a magnification of the high frequency part.

Each separate element in Figure 30a represents different resistances and charging components of the DSC where R_S is the substrate, contact and lead resistances of the solar cells. R_t is the transport resistance of electrons through the meso-porous TiO_2 network, which is in analogy with Eqs. 7 and 8 and is both light and potential dependent. C_μ is the chemical capacitance of the TiO_2 material and determines how much charge could be stored in the TiO_2 at every potential. The R_{ct} is the charge transfer resistance associated with recombination of electrons to the electrolyte across the TiO_2/Dye/electrolyte interface. A high recombination rate of electrons is reflected as a low R_{ct}, slow recombination kinetic on the other hand yields large R_{ct}. The dependences of the R_t and R_{ct} towards the C_μ are similar to each others, where an increase in the C_μ reflects an increase in the $E^*_{F,n}$ position of the TiO_2 yielding both lower R_t and R_{ct}.

Figure 30b shows impedance data measured for a liquid electrolyte DSC based on the sensitizing dye MP05 and the I^-/I_3^- redox electrolyte. The solar cell, measured at applied potentials and in darkness, shows two semi-circles representing the interface between the platinized counter electrode and the electrolyte (at low Z') and the interface between the TiO_2 and the electrolyte (at high Z'). The diffusion impedance is occurring at lower frequencies than measured here (up to 1 Hz) and is subsequently not measured. The intermediate part between the two semi-circles, clearly visible in the inset of Figure 30b, represents the R_t. It is now possible to rewrite Eq 9. to get the electron diffusion length as a function of the different impedance resistances, see Eq. 19.

$$L_D = L\sqrt{\frac{R_{ct}}{R_t}} \qquad \text{Eq. 19}$$

4.4 Characterization of solar cell materials

As well as characterization of complete solar cells, the characterization of each individual component is also crucial for the understanding and selection of materials for building DSC. This chapter deals with the most important characterization techniques which were applied to materials prior to DSC assembly.

4.4.1 Optical measurements (UV-VIS)

Absorption or transmittance spectroscopy is one of the simplest techniques available in a chemistry laboratory but versatile and powerful enough to warrant a closer explanation. The transmittance is the ratio of transmitted light through the sample and the incident light (Transmittance = I/I_0) where I is the transmitted light intensity and I_0 is the incident light intensity. To accurately determine the amount of absorbed light in a sample it is helpful to measure reflectance and absorption in an integrating sphere configuration. This approach is especially important when dealing with highly scattering samples, as for example with solar cells using scattering layers or reflecting contacts. Absorption spectroscopy is also used to determine the extinction coefficients of sensitizing dyes and to follow the relative change of oxidation as used in *Paper V*.

4.4.2 Electrochemistry

One of the most important characteristics for materials used in electronic devices is their electronically active levels. For a working DSC a photo-oxidized dye need to have a lower energetic level compare to that of the reducing species in the electrolyte, or HTM, to be able to be regenerated.[149]

Correspondingly, the photo-excited state of the dye has to have a higher energetic level than the conduction band of the TiO_2 to be able to inject electrons.[150] For example, meso-porous films of TiO_2 particles in a redox inactive electrolyte has a conduction band potential of -0.54 V vs. NHE at pH 7.[32,151]

These energy levels can be partly accessed through electrochemical measurements where the energy levels of the different materials are evaluated with respect to a common reference standard. Electrochemistry is usually carried out in a three electrode set-up with a working electrode, a counter electrode and a reference electrode for potential control. Current running through an electrochemical set up is of two types, either due to charge-transfer reactions (Faradaic) or due to charging effect (non-Faradaic) currents.[48]

One common technique used in electrochemistry is to linearly scan back and forth the potential in the electrochemical device and read the resulting current. This type of electrochemical measurement is called cyclic voltammetry (CV). Due to its simplicity and to obtain information about the electrochemical properties of different systems it is one of the mostly used experimental techniques in this thesis. Figure 31 shows a cyclic voltammogram on the sensitizer dye MP05 which has been attached to a meso-porous film of TiO_2. The supporting electrolyte was a solution of 0.1 M $LiClO_4$ in 3-methoxypropionitrile. The counter electrode was a platinum mesh while the reference was a silver/silver chloride electrode. The oxidation potential of MP05 was internally calibrated by using ferrocene.

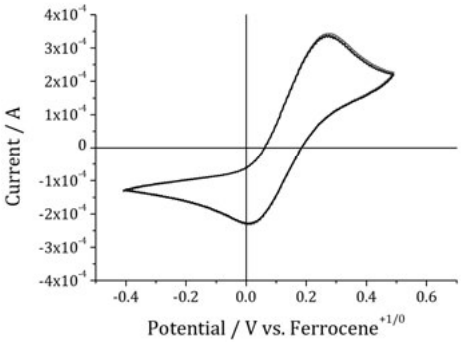


Figure 31: The first oxidation peak of the sensitizing dye MP05 attached on a meso-porous TiO_2 electrode as measured with cyclic voltammetry. The scan rate was 0.1 Vs^{-1}.

Electrochemistry could also be combined with absorption spectroscopy to measure the absorption spectra of electrochemically oxidized or reduced

species.[152] An example could be seen in Figure 32 where the absorption of a spiro-OMeTAD film was monitored while performing electrochemical measurements. The ground state absorption of spiro-OMeTAD has a peak at 400 nm while oxidized spiro-OMeTAD molecules have a complex absorption spectra with peaks between 420-770 nm and above 900 nm (see Figure 18).

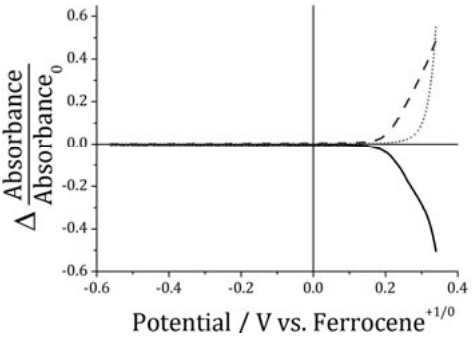


Figure 32: Spectroelectrochemistry on pure spiro-OMeTAD deposited on a FTO substrate. The changes in absorption of three spectral components were monitored as a function of a linear increase in potential, here internally calibrated versus ferrocene. 390 nm (black solid), 500 nm (dark gray dashed) and 900 nm (gray dotted).

From Figure 32 it is apparent that the spiro-OMeTAD oxidation peak at 500 nm is quite different from the one at 900 nm, indicating a potential difference of ~ 80 mV between the two species. The negative change in absorption at 390 nm corresponds to ground state bleach in spiro-OMeTAD as the oxidation process proceeds.

4.4.3 Conductivity measurements on IME

Interdigitated micro-electrodes (IME) are commercially available (ABTECH scientific) patterned electrode arrays with well defined narrow electrode spacing.[153] Spiro-OMeTAD and gold have shown to have negligible contact resistance both as a pure and doped material.[154] The resistance of pure spiro-OMeTAD is very high and in order to gain measureable voltage drops across an almost isolating resistor, the conduction length has to be very short and the cross-section area sufficiently large. The IME supplies both a reproducible substrate and a narrow conduction path on which the conductivity of spiro-OMeTAD can be measured.

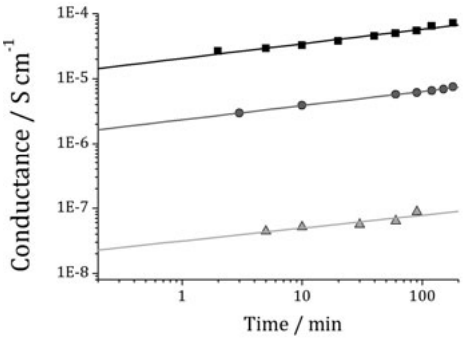


Figure 33: Electrochemical doping of solid films of spiro-OMeTAD containing different concentrations of Li-TFSI salt as measured on a gold plated IME. Pure spiro-OMeTAD (triangles), 10 mM Li-TFSI (circles) and 30 mM Li-TFSI (squares) measured in ambient air and light conditions.

Conductivity measurements were carried out on spiro-OMeTAD deposited on gold plated IME which are presented in *Paper V*. Figure 33, for example, shows how the conductivity of spiro-OMeTAD increases when adding different concentrations of the Li-TFSI salt but also how the conductivity continues rising when exposing the spiro-OMeTAD film to ambient air.

4.4.3 Carrier mobility using time-of-flight

A critical property of a solid-state hole transporting material is how well it transports charges. According to Eq. 10 in chapter 3.2, this property is determined by both the mobility of the charge carriers and the doping density of the material. The amount of charge carriers or holes in spiro-OMeTAD can be varied with doping and monitored through absorption spectroscopy as seen in the previous chapters. To measure the carrier mobility on the other hand requires other techniques. The most common techniques are organic field-effects transistors,[155] space-charge limited currents,[156] doping induced conductivity (CELIV),[157] and the time-of-flight (ToF) technique.[65,106,157-159]

In the ToF technique the velocity distribution of photo-generated charge carriers is measured as they move through the material of interest. Organic semiconductors and polymers have been extensively investigated using ToF techniques, where the influence of molecular structure and doping have both been shown to influence the carrier mobility.[106,108,160-161] The sample geometry for ToF measurements usually consists of the material of interest sandwiched between two metal contacts of which one needs to be transparent. The selection of contact metals also determines if the device set-up measures the carrier mobility of holes or electrons. During the operation a potential is applied to the transparent electrode while the other contact is grounded

through a sensing resistor (R_{sens}). Charges are generated by a nano-second laser pulse, absorbed by either the transporting material or a charge generation layer (Q). Optimally, the free photo-generated charge should be formed as a narrow band in order to avoid ill-defined current transients.

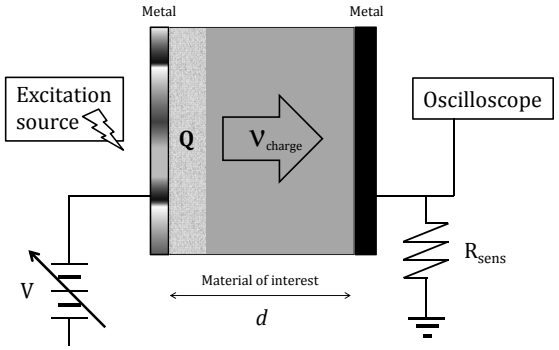


Figure 34: A schematic picture of the experimental set-up of a time-of-flight technique.

The formed free charge can now move, from contact to contact, in the material of interest because an electrical field is developed by the application of a potential. It is this electrical field which is the driving force for charge to transverse across the sample. Photo-generated charges are collected through the measurement circuit where the current produce a measureable voltage drop when passing the sensing resistor. The typical experimental set-up can be seen in Figure 34, where v_{charge} is the velocity of the free charge carriers and *d* is the film thickness, usually in the µm range. The charge velocity is recorded on an oscilloscope from which the mobility of the material can be obtained when knowing the film thickness.

5. Results

Previous chapters have identified the current limitations in both liquid and solid-state DSC as well as the necessary background information to interpret the results in the following chapter. The aim of this doctorial thesis is to increase the understanding of the operating fundamentals of the solid-state DSC, and to propose and investigate new ways to overcome limitations in the solid-state DSC device. The following subchapters will each deal with one paper included into this thesis, introducing the reader to some of the most important and interesting findings.

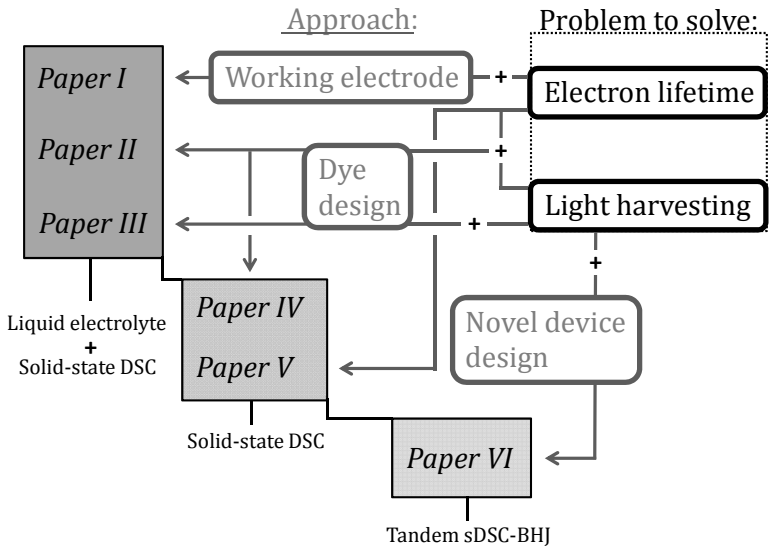


Figure 35: A schematic representation of the two main problems/limitations associated with increasing conversion the efficiency in solid-state DSC. Different approaches were employed to deal with these limitations resulting in *Paper I-VI*.

Core-shell structures for DSC are presented in chapter 5.1 and it is associated with *Paper I*, dealing with the low electron lifetime of solid-state DSC and how to improve the charge collection efficiency in these devices. The next paper investigates the differences in highly efficient liquid and solid-state DSC with regards to the dye structure and electron lifetime, chapter 5.2 and *Paper II*. *Paper III*, chapter 5.3, on the other hand examines the perylene dye molecular structure which is working efficiently in the solid-state DSC

configuration but not in the liquid electrolyte system. A new molecular core structure was investigated in *Paper IV*, chapter 5.4 and how these similar structures can yield very different device efficiency in solid-state DSC was discussed. *Paper V*, chapter 5.5, deals with the effects of oxygen on the solid-state DSC based on spiro-OMeTAD. The problem with low light absorption was addressed in the last paper by pioneering a novel device structure based on a tandem cell consisting of an evaporated bulk heterojuction solar cell on top of a solid-state DSC, see chapter 5.6 and *Paper VI*.

5.1 Core-shell structures for DSC (*Paper I*)

Solid-state DSC based on spiro-OMeTAD has lower electron lifetimes compared to similar devices having an electrolyte based on the I^-/I_3^- redox couple.[118] To increase the electron lifetime or to increase the effective electron diffusion length it is possible to adopt several approaches, for example to use surface protecting additives such as 4-tert-butyl pyridine,[162] or different phosphonic acids.[80-81] Another approach includes research efforts to find new metal-oxide materials and geometries to use in the DSC. Since the beginning metal oxides like SnO_2, [113,146,163] ZnO,[30,164] and Nb_2O_5 alongside with TiO_2 were employed in DSC.[165] These materials have been investigated in various geometric structures such as wires,[166] tubes,[167] and hollow-spheres,[168] but also as layered forms where one metal oxide is coated on top of another material, the core-shell structure.[135]

Two main approaches can be discerned, using insulating metal oxides as barrier layers to reduce recombination or to use two wide band gap semiconductors as core-shell to utilize the separate electronic properties of the materials.[135,168] Core-shell structures for DSC using two wide band gap material was first reported in literature by Tennakone *et al*.[169] in 1999 using tin oxide and zinc oxide (core-shell). Since then SnO_2-TiO_2,[135,170] TiO_2-ZnO,[171] TiO_2-$SrTiO_3$,[172] and other configurations have been reported in literature. Core-shell structures using an insulating metal oxide includes work done with Al_2O_3,[173] SiO_2,[174] MgO,[175] ZrO_2,[137] and Y_2O_3.[135]

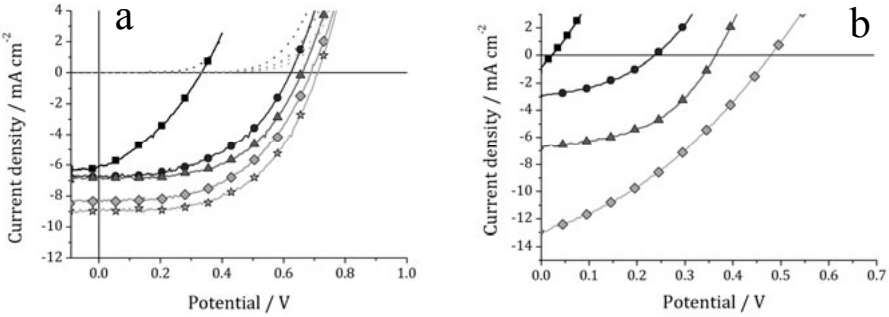


Figure 36: J-V curve of a liquid electrolyte DSC based on I^-/I_3^- and the sensitizer dye D35 (left, a) and J-V curve of solid-state DSC based on spiro-OMeTAD (right, b). Pure SnO_2 electrode (square), SnO_2 + 10 cycle TiO_2 (circle), SnO_2 + 20 cycle TiO_2 (triangles), SnO_2 + 30 cycle TiO_2 (diamonds) and SnO_2 + 40 cycle TiO_2 (stars). All cells were illuminated with 1000 Wm^{-2}.

Paper I investigates the application of a meso-porous SnO_2-TiO_2 core-shell structure for liquid and solid-state DSC. The aim is to transfer photo-injected electrons from the surface of the shell material to the core material in order to avoid electron-hole recombination. The driving force for the electron transfer step, between the oxide materials, would be the lower conduction band edge of SnO_2 compared to TiO_2. When the electron has moved into the SnO_2 core material it is free to move to the FTO contact. For the electron to recombine with oxidized species in the electrolyte it has to overcome the potential barrier between the $E_{F,n}^*$ and the conduction band edge of TiO_2. This approach might not be appropriate for liquid electrolyte DSC based on the I^-/I_3^- redox electrolyte since for meso-porous network of SnO_2 sufficient large electron diffusion lengths has been demonstrated.[146]

The solid-state DSC on the other hand, as well as other redox system, has yielded dismal performances using pure SnO_2 working electrodes and spiro-OMeTAD, see black square in Figure 36b. The main reason for the lacklustre performance of solid-state DSC using SnO_2 stems from the much lower conduction band of SnO_2, which is about 0.4 V lower than the conduction band of TiO_2.[32,146] This lower conduction band edge yield lower open-circuit potential as could be seen for the pure SnO_2 in Figure 36a and therefore also lower efficiency. SnO_2 has a higher conduction band mobility than TiO_2, a property which might yield faster electron transport in meso-porous structures based on SnO_2 compared to TiO_2.[163,159] It is noted that the photo-current for the solid-state DSC with 30 cycles TiO_2 ALD coating is very high. The reason for this is still unknown and without being able to correlate the photo-current density with the integrated IPCE spectra it is not possible to rule out excessive photo-currents due to edge effects from improper masking. [176]

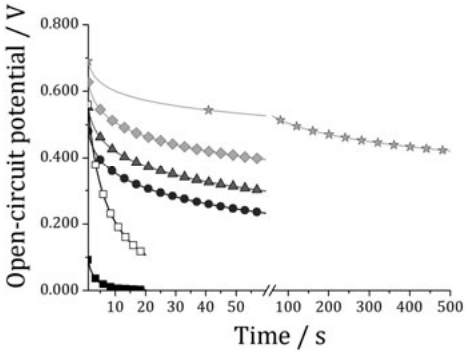


Figure 37: V_{oc} decay measurements of liquid electrolyte DSC based on working electrodes made from pure SnO_2 (black square) and pure TiO_2 (open square) as well as core-shell structures based on SnO_2 + 10 cycle TiO_2 (circles), SnO_2 + 20 cycle TiO_2 (triangles), SnO_2 + 30 cycle TiO_2 (diamonds) and SnO_2 + 40 cycle TiO_2 (stars). All cells were illuminated with 1000 Wm^{-2} for 10 seconds for charging. Note the different scale of the x-axis at the break at 60 seconds.

Figure 37 illustrate V_{oc} decay measurements performed on liquid electrolyte DSC. This technique is using a very similar method as the electron lifetime measurement presented in chapter 4.3.3 with the difference that the photo-voltage decay is measured under darkness with no light modulation. Figure 37 shows how the decay of the photo-voltage is extended when using SnO_2-TiO_2 core-shell structures for liquid electrolyte DSC compared to pure working electrode materials. This is evidence for electron transfer from the TiO_2 shell to the SnO_2 core and that electrons are trapped in the core material under open-circuit condition. When switching the core-shell device from open-circuit conditions to short-circuit condition the trapped charges are quickly collected at the external circuit, showing that the charges present in the SnO_2 core materials are indeed mobile.

In this paper a novel method of producing high quality SnO_2-TiO_2 core-shell structures was presented. Solid-state DSC has a lower electron lifetime compared to liquid electrolyte DSC based on the I^-/I_3^- redox couple. Increasing the electron lifetime is thus a crucial step in improving the device conversion efficiency in these types of devices. The electron lifetime in these SnO_2-TiO_2 core-shell devices are very long compared to the pure working electrode material, which is also reflected in the increase in device performance of both solid-state and liquid DSC.

5.2 Efficient dyes for DSC (*Paper II*)

Dye molecules based on triphenylamine donors, thiophene linkers and 2-cyanoacrylic acid as acceptor-anchoring groups have previously been pre-

sented by Hagberg *et al.*[177-179] One of the most efficient sensitizing dyes in this family is the D35, the molecular structure is shown in Figure 9, which has proven to work very efficiently in both liquid electrolyte and solid-state DSC. Figure 38 shows the currently best J-V curve of a solid-state DSC based on D35 and spiro-OMeTAD with an efficiency of 4.65 % at 1000 Wm^{-2}.[129]

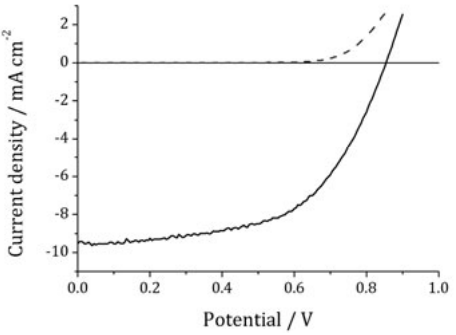


Figure 38: The current record efficiency of an optimized solid-state DSC based on D35 and spiro-OMeTAD. Figure adapted from reference.[129]

D35 was early on chosen to be optimized and used as a benchmarking dye for standardizing the performance of solar cell work done in this thesis. Using a benchmarking dye is important when doing research in the field of DSC since small variations in material quality or mistakes during the solar cell assembly steps might influence heavily the overall result of an experiment.

The molecular structure of D35 consists broadly of two alkoxy groups substituted on a triphenylamine unit together with one thiophene linker-anchoring group. By substituting one alkoxy group with an identical linker-anchoring group, it is possible to investigate the influence the anchoring group has on the dye and on the complete performance of DSC devices. This approach has previously been reported to increase both the extinction coefficient of similar dyes as well as the efficiency.[180]

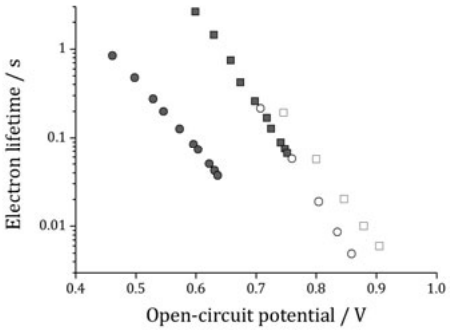


Figure 39: Electron lifetime as a function of the open-circuit potential in liquid electrolyte DSC based on I^-/I_3^- (filled symbols) and on DSC based on spiro-OMeTAD (open symbols). DSC devices made with D35 (squares) have longer electron lifetime at equal V_{OC} compared to M14 (circles).

The M14 dye and its similarities in molecular structure to D35 can be seen in Figure 9. The extended conjugation in M14, which is the result of exchanging one alkoxy group with an additional thiophene linker-anchoring group, does indeed increase the extinction coefficient of M14 compared to D35. This increase in extinction coefficient from $3.1 \cdot 10^4$ $M^{-1}cm^{-1}$ (500 nm) in D35 to $5 \cdot 10^5$ $M^{-1}cm^{-1}$ (504 nm) in M14 does influence the generated photocurrent density in solid-state DSC devices but not in the liquid electrolyte DSC. The reason for this dissimilarity is the difference in thickness of the working electrodes used for solid-state (2 μm) and for liquid electrolyte (10 μm) and thus their LHE.

In both liquid and solid-state DSC D35 outperforms M14 and although the difference in efficiency between the dyes are smaller for solid-state than for liquid electrolyte DSC the reason for the lower efficiency is the same. Figure 39 shows the electron lifetime of D35 and M14 in both the liquid electrolyte and the solid-state DSC configuration. Comparing the electron lifetime of D35 and M14 at equal V_{oc} in liquid electrolyte DSC the devices comprising D35 exhibit a 45 times faster electron recombination lifetimes compared to the devices comprising M14. A difference in electron lifetime is also measured between D35 and M14 in the solid-state configuration but the difference is much smaller: only a 6 times faster electron recombination was observed for D35 compared to M14.

The reason for the increase in electron recombination seen for M14 compared to D35 is not known. It has previously been proposed that dye molecules including thiophene or pyridine units might coordinate iodine species close to the TiO_2 surface and therefore increase their chance of capturing electrons from the meso-porous TiO_2 network.[181]

In this paper two structurally similar dyes, the D35 and M14, were investigated. The M14 dye had two anchoring groups, rendering it a larger extinction coefficient than D35 but also a lower electron lifetime. The lower electron lifetime is suspected to lower the V_{oc} and thus preventing M14 to supersede D35 in conversion efficiency.

5.3 A perylene dye in liquid and solid-state DSC (*Paper III*)

The perylene molecular structure, which consists of two naphthalene units joined together at peri-position, is a well known core chromophore. This molecular structure has two characteristics which make it a suitable candidate to use as a sensitizer core moiety for DSC applications. It has an excellent photo-stability and high extinction coefficient.[182-183] Many different variations of this molecular structure have been employed successfully as a sensitizer in DSC applications.[184-186] The perylene based dye structure ID176, see Figure 9, has proven to work efficiently in solid-state DSC based on spiro-OMeTAD. Its high extinction coefficient of $2.5 \cdot 10^4$ $M^{-1}cm^{-1}$ at 590 nm and its broad absorption spectra makes it an excellent candidate dye for yielding high efficiency DSC.

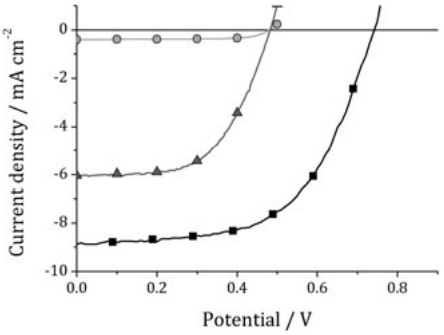


Figure 40: J-V curves using the perylene dye ID176 in solid-state DSC with spiro-OMeTAD (square) and in liquid electrolyte DSC without (triangles) and with (circles) the additive 4-tert-butyl pyridine.

It was rather surprising to discover that ID176 performs less efficient in liquid electrolyte DSC based on the I^-/I_3^- redox mediator, compared to solid-state DSC. Figure 40 shows how a solid-state DSC device made from 1.7 µm thick TiO_2 electrodes is more efficient than liquid electrolyte made from a working electrode of more than 8 µm thickness. It also shows how the short-circuit current in the liquid electrolyte DSC almost ceases when the

TiO_2 conduction band edge is increased by addition of the solar cell additive tBP into the electrolyte.

Table 2. *Solar cell performance data of liquid and solid-state DSC using ID176*

Sample	V_{oc} / V	J_{sc} / $mA \cdot cm^{-2}$	FF / %	η / %
Liquid with tBP	0.480	0.40	71	0.14
Liquid without tBP	0.485	6.05	57	1.68
Solid with tBP	0.745	8.90	58	3.81

Table 2 above shows the solar cell device data recorded for the DSC in Figure 40. Similar device results are also reported in paper III, where the diffusion length of electrons in the liquid electrolyte DSC was determined to be higher than 9-13.5 μm. Because of this, it was possible to rule out lower charge collection efficiency in the liquid electrolyte DSC based on ID176 as a reason for the lower short-circuit current seen in these devices. Studies on the injection and regeneration dynamic of ID176 utilizing ultra-fast spectroscopy has been published by Cappel *et al*.[187-189] showing that ID176 was able to inject photo-excited electrons into TiO_2 in the absence of organic solvents but not able when a liquid electrolyte is present, like in the I^-/I_3^- electrolyte.

In this paper was a new perylene dye, ID176, demonstrated in both liquid and solid-state DSC. The perylene dye performed well in solid-state DSC but yielded poor efficiencies in liquid electrolyte DSC. It was also found that the photo-current density depended on the position of the TiO_2 conduction band, as varied by electrolyte additives like tBP.

5.4 Phenoxazine dyes for sDSC (*Paper IV*)

Investigating series of organic dye molecules based on a systematic change in molecular structure is a powerful strategy to obtain an understanding of the structure-function relationship in complex systems such as the solid-state DSC. The phenoxazine core, as seen in Figure 41, is a well known chromophore which has been used both as a laser dye and staining dye.[190-191] Dyes based on the phenoxazine core and the structurally very similar phenothiazine core have just recently been described to give high conversion efficiencies as sensitizer dyes in liquid and solid-state DSC.[192-194]

The phenoxazine core moiety can easily be modified at the three positions seen in Figure 41 yielding the dyes MP03, MP05, MP08 and MP13. These dyes have been optimized both for the liquid electrolyte DSC and for the solid-state DSC based on spiro-OMeTAD, see *Paper IV*.[194]

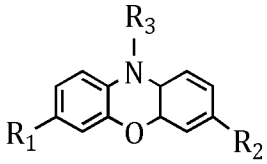


Figure 41: The phenoxazine core structure which has been modified at position R1, R2 and R3 to yield the MP-dyes.

The molecular structures of these dyes are shown in Figure 9 and the synthesis route has been previously described.[194] When a dye molecule fulfil the basic requirements for a dye to work in DSC devices, such as the right HOMO/LUMO energy levels and a high oscillator strength, it is possible to try to fine-tune the surface protecting properties of the dye. This is often done by introducing alkoxy substituents to the chromophore moiety to reduce the contact between the electrolyte and the TiO_2 surface, reducing the electron recombination.[28,41,128,179,192] Looking at the structure of the MP dyes in Figure 9 the increased substitution of MP05 and MP03 compared to MP13 can be noted. The relative low LHE of these dyes, which in *Paper IV* is reported to be 19-29 % between 350-1000 nm, is also addressed by increasing the conjugation. In MP08 a furan ring was introduced into the linker group in a successful attempt to extend the conjugation and to red-shift the absorption spectrum of the dye.

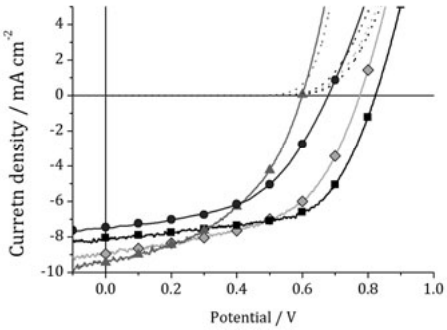


Figure 42: Current density-voltage measurements of solid-state DSC devices based on spiro-OMeTAD and measured under 1000 W m^{-2} (AM1.5G) using MP03 (diamonds), MP05 (squares), MP08 (triangles) and MP13 (circles). The dotted curves represents the dark J-V.

The resulting J-V curves of solid-state DSC devices based on the MP-dyes and spiro-OMeTAD can be seen in Figure 42. It shows how the photocurrent is proportional with the LHE of the different dyes while the V_{oc} depend both on the electron lifetime rate constant and the change in a chemical dipole induced shift of the TiO_2 conduction band.

In this paper a series of dye molecules based on the phenoxazine core was investigated. The electron lifetime and the V_{oc} of solid-state DSC devices based on these dyes were found to vary with the degree of substitution. Inclusion of protecting alkoxy groups on the phenoxazine core moiety increased both the electron lifetime, FF and V_{oc}.

5.5 Effects of oxygen in sDSC (*Paper V*)

Since spiro-OMeTAD was successfully introduced as a hole transporting material in solid-state DSC in 1998 device efficiency has increased from 0.74 % to more than 7 %.[27,29] This order-of-magnitude increase in efficiency has been the result of optimizing the devices and screening new sensitizers rather than an increased understanding of the operating mechanisms in the solid-state system. It is generally acknowledged that the lower device efficiency of solid-state DSC based on spiro-OMeTAD derives from a low penetration of the HTM into the pores of the meso-porous TiO_2 network as well as a lower electron lifetime.[111 118,123] Studies of this penetration of spiro-OMeTAD into the meso-porous working electrode, or pore-filling as it is generally termed, have just started to draw some quantitative relationships between device efficiency and pore-filling.[111-110,123,125] The lower electron lifetime in solid-state DSC on the other hand is not so well understood. It has been proposed that the electron screening in the TiO_2 might not work as efficient in the solid-state DSC device as it does in liquid high ionic strength electrolytes. [118]

Early in the development of solid-state DSC a chemical oxidizer was added to the spiro-OMeTAD matrix in order to increase the conductivity of the HTM.[27] This was believed to be necessary due to the high serial resistance of pure un-doped spiro-OMeTAD but was later proven wrong by the discovery of efficient un-doped solid-state DSC devices.[195,28] Regardless if a solid-state DSC device is built with a dopant or not they all have the Li-TFSI salt included into the spiro-OMeTAD matrix. The Li salt has been described as a redox inactive species that increase the conductivity of spiro-OMeTAD by increasing its hole mobility.[77] As could be seen in Figure 33 the Li-TFSI salt does indeed increase the conductivity in a film of spiro-OMeTAD.

It has also been known for quite some time that oxygen plays an integral part in the operation of solid-state DSC based on spiro-OMeTAD but the reason for this has not been clear.[196,128] *Paper V* investigates the effects ambient air/oxygen have on the device performance of solid-state DSC as well as exploring the effects gaseous molecules have on pure spiro-OMeTAD.

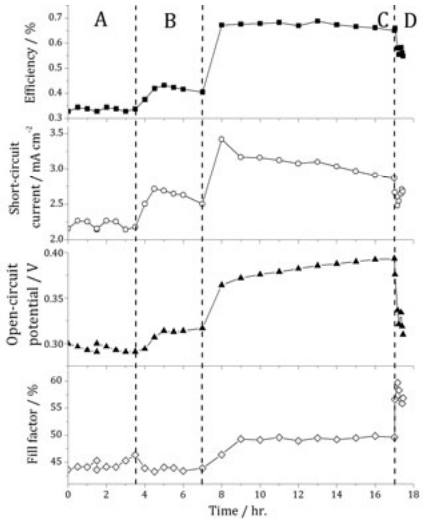


Figure 43: Evolution of the solar cell characteristics of a solid-state DSC device without tBP under different air pressures. After the solar cell had stabilized at $1 \cdot 10^{-7}$ mbar, repeated current-voltage measurements were performed under 860 W m^{-2} illumination. The dashed lines indicate when the air pressure was changed: $1 \cdot 10^{-7}$ mbar (region A), $1 \cdot 10^{-3}$ mbar (B), $1 \cdot 10^{+3}$ mbar (C) and back to $1 \cdot 10^{-3}$ mbar (D).

Figure 43 shows how differences in ambient air pressure influence the device performance of a solid-state DSC based on spiro-OMeTAD. Going from a low pressure to high pressure leads to an increase in all solar cell device parameters and large increases in conversion efficiency. By fitting solar cell J-V data to the one-diode model it is possible to obtain additional information which can help in narrowing down where the increase in efficiency stems from. Using this method a photo-dependent shunt conductivity, a leakage of current from the solar cell was revealed, which shuts down when storing the solid-state DSC devices under ambient atmosphere conditions. This storage phenomenon together with a reduction in the serial resistance of the solid-state DSC device rendered the conversion efficiency almost 1 percentage higher after storage. The decrease in serial resistance could be caused by two different effects: An increase in the number of charge carriers in the spiro-OMeTAD as well as an increase in the spiro-OMeTAD hole mobility when exposing the solar cell to ambient air.

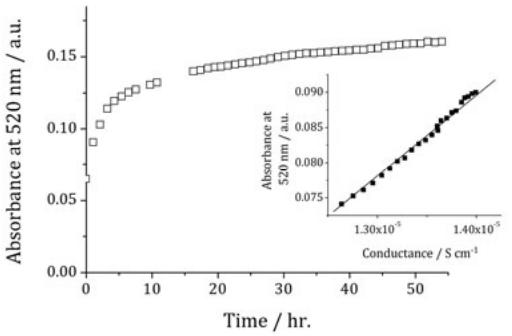


Figure 44: Change in absorption at 520 nm of a spiro-OMeTAD film containing Li-TFSI and tBP when stored under an ambient air atmosphere. Inset: the relation between absorbance at 520 nm and the conductivity of the film.

Figure 44 shows how the absorbance of oxidized spiro-OMeTAD, as followed by UV-VIS absorption spectroscopy at 520 nm, correlate with the conductance of a film of spiro-OMeTAD containing Li-TFSI and measured using a IME, as explained in Chapter 4.4.3. These changes in conductivity of spiro-OMeTAD with time have never been observed before and are likely to be the cause of the increase in device performance observed after storing devices under ambient atmosphere conditions for a certain period of time. The mechanism for this oxidation is not yet understood and further experiments are needed. The working hypothesis have been and still is that the oxidation of spiro-OMeTAD proceeds through a photo-excitation of spiro-OMeTAD, in which it passes on an electron to either an oxygen or water molecule while the oxidized molecule is stabilized by the Li-TFSI salt.

In this paper the effects of ambient air and oxygen on spiro-OMeTAD and on a solid-state DSC based on spiro-OMeTAD were investigated. Solar cells become significantly more efficient when exposed to ambient air after solar cell assembly. This effect was explained by a reduction in serial resistance in the solar cell device as well as an increase in the electron recombination lifetime, showing that not only preparation methods are important for obtaining efficient solar cells but also the treatment of the devices after assembly.

5.6 Tandem bulk heterojunction – solid-state DSC (*Paper VI*)

The general purpose of tandem solar cell is to place two solar cells on top of each other, connected in serial, to be able to harvest more light while keeping the area the same. When utilizing two light absorbing materials with different band gaps and complementary absorption spectrum it is possible

increase the maximum theoretical conversion efficiency of the solar cell device beyond the maximum value set by the Shockley-Quiesser limit.[114] Organic tandem solar cell devices have previously been made from all-solution processed polymers reaching efficiencies of 6 %.[197] Evaporated small molecular organic solar cells reach even more impressing efficiencies of 8.3 %.[8]

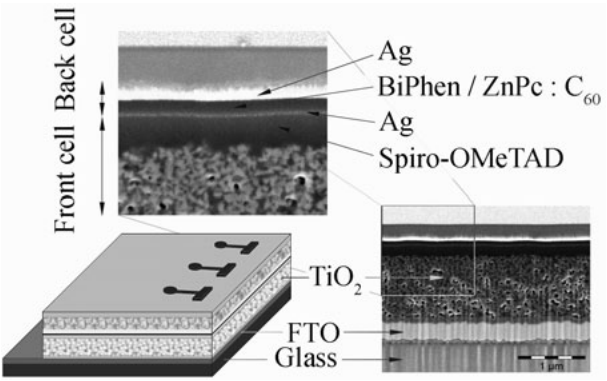


Figure 45: A schematic representation of the complete tandem solar cell based on a solid-state DSC made with spiro-OMeTAD and D102 together with an evaporated small molecular bulk heterojunction solar cell based on ZnPC and C_{60}. A cross-section scanning electron microscopy picture shows the individual components of the tandem solar cell device.

Since the two half cells of the tandem solar cells are connected in series they should ideally generate the same photo-current density since the overall current-density will be determined by the worst performing half cell. The photo-voltages on the other hand should add up. Thus, balancing the photo-current given by each half cell is one of the most important parameters when deciding which half cells to combine and how. The photo-current in each half cell is determined by, as for all other solar cells, how many photons reach the active area of the solar cell. The difference between the tandem cell and a regular single junction device is that the first half cell, or front cell, filters all the incoming light which could reach the second half cell, or the back cell. This filter effect plays an important role in deciding the optimum optical density of the first half cell, which in *Paper VI* is determined by the thickness and extinction coefficient of the dye used for the solid-state DSC. *Paper VI* is the first reported tandem solar cell based on solid-state DSC as the first half cell with the evaporation of a small molecular bulk heterojunction solar cell as the second half cell, the preparation method was previously described in chapter 4.1.3. Figure 45 shows a schematic representation of the complete tandem cell device with all layers indicated as well as a cross-section SEM picture where most of the individual layers can be seen.

The cross-section picture as seen in Figure 45 clearly shows the different components of the solid-state DSC while the different components of the BHJ solar cell is less clear mainly because of the relative difference in thickness between the devices. The silver recombination layer can be distinguished as a bright thin line on top of the overstanding layer of spiro-OMeTAD. The purpose of this recombination layer is to act like a catalyst for the recombination between electrons generated in the BHJ solar cell and holes generated in the solid-state DSC and transported through the spiro-OMeTAD. Figure 46 shows the outstanding J-V performance of these tandem solar cell devices under 1000 W m^{-2} illumination, showing both a very high photo-voltage as well as retaining photo-current densities around 10 mA cm^{-2}, similar to the solid-state DSC halfcell.

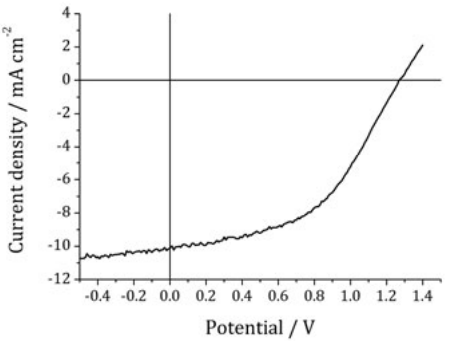


Figure 46: The J-V characteristics of 6% efficient tandem solar cell based on a solid-state DSC as first half cell and a small organic molecule evaporated bulk heterojunction solar cell as the second half cell.

In the IPCE spectra of these tandem solar cell devices, shown in *Paper VI*, it is apparent that the IPCE value of the BHJ half-cell device is lower when incorporated into a tandem device structure, compared to the single device. This effect can be explained by a disruption of the internal optical interference pattern within the ZnPC:C_{60} layer, an effect which due to the thickness of the BHJ solar cell (~70 nm) can play an integral part.[198]

In this paper a novel tandem solar cell, based on a solid-state DSC and an evaporated BHJ solar cell, was demonstrated. The efficiency of these devices reached a high value of 6 %, opening up a new route to harvest more photons and to circumvent the limitations of having a single absorber.

6. Concluding remarks

Over the last 10 years or so the conversion efficiency of solid-state DSC has increased an order of magnitude. Continuing this increase in the future will prove to be more and more elusive, especially if the increase in efficiency is not followed by a greater understanding in the operating principals behind the DSC. So far the conversion efficiency of solid-state DSC suffers from two main drawbacks compared to the liquid electrolyte DSC. Low light absorption due to limitation in working electrode thickness and low electron lifetime, affecting solar cell parameters such as the short-circuit current density, fill factor and V_{oc}. This doctorial thesis has addressed both these problems through different technological approaches. For example, the molecular structure of the sensitizing dye was evaluated in *Paper II* and *IV* where the molecular structure is influencing both the electron lifetime and the light harvesting capabilities of the solar cell. In *Paper I* the working electrode material was modified to increase the electron lifetime in both the liquid and solid-state DSC while *Paper VI* introduced a novel tandem solid-state solar cell concept to extend the light harvesting power of this type of solar cells.

For future work it would be interesting to further explore new hole transporting materials, especially those which can be melt-infiltrated into the mesoporous TiO_2 structure, described by Fredin *et al*.[199] Another question that needs to be addressed, at least in my opinion is how the molecular ordering and coverage of the sensitizing dye on the TiO_2 surface affects the electron recombination lifetime.

Sammanfattning på svenska

Inledning

Människors behov av energi växer för varje år och att fylla detta behov med hållbar och miljövänlig energi är en av århundradets viktigaste utmaningar. Under 2009 användes det i hela världen ungefär $1.9 \cdot 10^4$ TWh elektrisk energi och hela 80 % av denna energi producerades från icke-förnyelsebara källor.[1] En kombination av ökad efterfrågan av elektricitet och en oro över global uppvärmning har drivit på utbyggnaden av förnyelsebara energikällor under de senaste åren.[2] Till kategorin förnyelsebara energikällor brukar vatten-, vind- och vågkraft räknas men även geotermisk- och solenergi. Mogna tekniker som vatten- och vindkraft står just nu för den största ökningen i kapacitet medan solenergi är den källa som beräknas ha störst utbyggnadskapacitet, om och när tekniken blir kostnadseffektiv. För att exemplifiera den enorma potential solenergin representerar är det möjligt att göra ett litet räkneexempel: Jorden mottar varje dygn i genomsnitt mellan 3-6 kWh per kvadratmeter. Om en yta som motsvarar ca 1.4 % av Saharas öken skulle täckas med 10 % effektiva solceller så skulle det ensamt producera tillräckligt med elektricitet för att tillgodose hela världens behov.

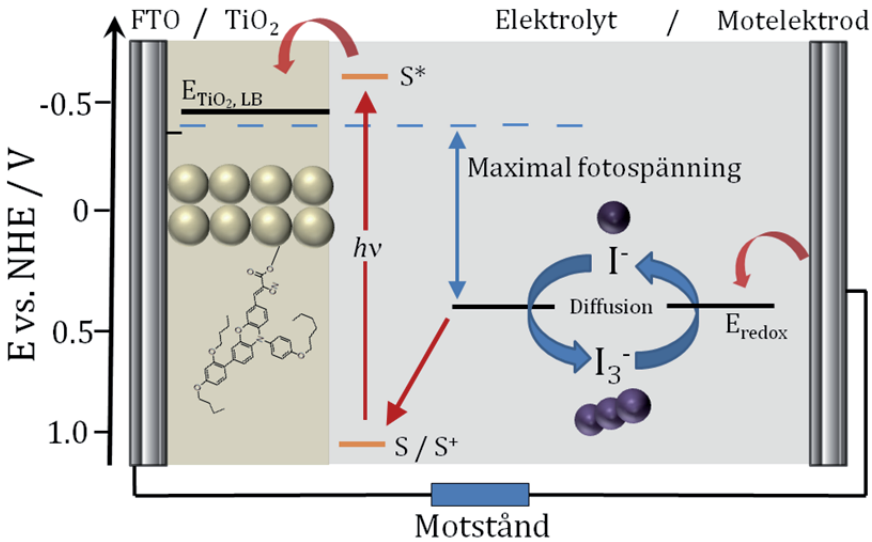
Solceller

Solceller omvandlar den elektromagnetiska energin från solen till användbar elektrisk energi. Denna effekt upptäcktes redan 1839 av den franske fysikern Edmond Becquerel men det tog över hundra år innan solcellernas egenskaper fann ett användningsområde utanför vetenskapen.[6] Det var kunnandet från transitorindustrin som gjorde att AT&T's Bell Laboratories på 1950-talets började använda halvledarmaterialet kisel för att bygga de första verkligen användbara solcellerna.[7] De första solcellerna som producerades var väldigt dyra och användes främst inom rymdindustrin. Kostnaden för att producera solceller som baseras på kisel har minskat men även andra material har börjat användas för att bygga solceller. Kiselsolceller har för närvarande en effektivitet på 20-25 % medan gallium-arsenik solceller har en effektivitet över 30 %. Tunnfilmssolceller av bland annat kadmium-tellurid kommer upp i 17 %.[8] Organiska solceller är ett relativt nytt forskningsfält som har ökat kraftigt de senaste 20 åren. Organiska solceller byggs av organiska halvle-

darmaterial där fokuset ofta ligger på att producera billigare solceller än vad som är möjligt med oorganiska solceller.

Fotoelektrokemiska solceller

En typ av hybridsolcell vars intresse har vuxit mycket de senaste åren är den fotoelektrokemiska solcellen eller som den också kallas, färgämnes-sensiterad solcell (DSC). Denna solcell demonstrerades av Brian O'Regan och Michael Grätzel 1991 med en effektivitet på 7 % och har sedan dess ökat i effektivitet till mer än 12 %.[13,22] Den färgämnes-sensiterade solcellen är byggd på n-typ halvledarmaterialet titandioxid (TiO_2), ett material som är både billigt, kemiskt stabilt och ogiftigt. Av detta material byggs ett meso-poröst TiO_2 skelett upp som måste färgas in med ett färgämne för att kunna absorbera solens energi. En reduktions-oxidations elektrolyt som oftast består av jodid och trijodid (I^-/I_3^-) infiltreras in i den meso-porösa TiO_2 elektroden, denna elektrolyt är ansvarig för att transportera laddningar mellan motelektroden och det foto-oxiderade färgämnet. Figur 1 visar en schematisk bild över hur en färgämnes-sensiterad solcell fungerar och hur den är uppbyggd.



Figur 1: En schematisk representation över hur en färgämnes-sensiterad solcell är uppbyggd samt de viktigaste energinivåerna som är aktiva i solcellen.

Processen för att generera elektrisk energi från en DSC består i flera steg. I Figur 1 ovan representerar *S* de energinivåerna i färgämnet som är viktiga för solcellens funktion. När solens ljus faller in på solcellen genom de genomskinliga glassubstraten som solcellen byggs upp på, kan fotonerna ab-

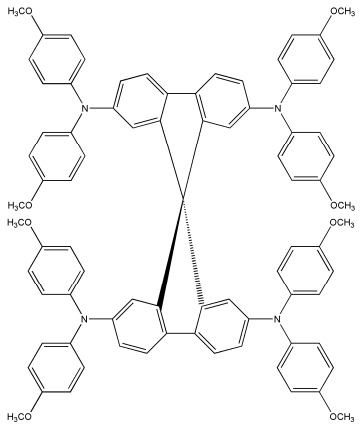
sorberas av färgämnet och en elektron exciteras från grundtillståndet i färgämnet, S, till det exciterade tillståndet, S*.

Det exciterade färgämnet, S*, injicerar en elektron till TiO_2 och där med har en laddningsseparation skett, en positiv laddning har bildats på färgämnet och en negativ laddning har injicerats till TiO_2. Färgämnets oxiderade tillstånd, S^+, kan nu genomgå en reduktion genom att ta en elektron från en I^- molekyl i elektrolyten. Det är potentialskillnaden mellan elektronen som befinner sig i TiO_2 med den elektrokemiska potentialen av elektrolyten som utgör grunden för den fotospänning som en DSC kan ge. Strömmen genereras i solcellen genom att den exciterade elektronen rör sig igenom TiO_2 med en diffusionsprocess tills den når den externa kontakten som utgörs av det ledande glaset (FTO). När kretsen till solcellen är sluten kan elektronen förflytta sig från arbetselektroden, över motståndet till motelektroden där den kan reducera en I_3^- molekylen till I^- och därmed är solcellen fullständig.

Effektiviteten av solcellen bestäms genom att multiplicera fotospänningen (volt) med fotoströmmen (ampere) som ger effekten (watt). Den avgivande elektriska effekten kan nu divideras på den inkommande elektromagnetiska effekten och resultatet är solcellens effektivitet i procent. När solcellers effektivitet är testade under laboratorieförhållanden är det vanligt att ljuskällan som används har en intensitet på 1000 W m^{-2}, ett värde som är nära solens intensitet en molnfri sommardag.

Fastfas färgämnes-sensiterade solceller

Färgämnes-sensiterade solceller som innehåller en vätska som elektrolyt har problem med att den kan läcka ut eller förångas. Dessutom har I^-/I_3^- elektrolyten problem med överpotentialer vid reduceringen av färgämnet. Sammantaget gör dessa problem att ett material i fastfas skulle vara att föredra över en vätskeformig elektrolyt. 1998 upptäcktes ett material av Bach *et al*. som uppfyllde kraven för att kunna bygga fastfas DSC.[27] Den kemiska strukturen hålledaren 2,2’,7,7’,-tetrakis(N,N-di-p-metoxyfenyl-amin)-9,9’,-spirofluoren (spiro-OMeTAD) kan ses i Figur 2.



Figur 2: Den kemiska strukturen för hålledaren 2,2',7,7',-tetrakis(N,N-di-p-metoxypenyl-amin)-9,9',-spirofluorene (spiro-OMeTAD).

Trots att materialet initialt resulterade i ganska dåliga solceller med en effektivitet på 0.7 % så ökade effektiviteten snabbt och ligger för närvarande på mer än 7 %.[27,29] Diskrepansen i effektiviteten mellan elektrolyt och fastfast solceller beror främst på två saker. Fastfas solceller har en betydligt snabbare elektron-hål rekombinering än vad en elektrolyt DSC har. Detta gör att fotoströmmen blir lägre i fastfas solcellerna som också därmed får en lägre effektivitet. Den andra anledningen är att hålledarmaterialet måste infiltreras in i de små porer som utgörs av det meso-porösa TiO_2 nätverket.[125] För den bästa fastfas DSC har den optimala tjockleken av TiO_2 filmen experimentellt bestämts till ungefär 2 mikrometer (μm), detta kan jämföras med tjocklekar på mer än 10 μm för elektrolyt DSC. I denna relativt tunna TiO_2 film så absorberas inte tillräckligt med fotoner och därmed blir fotoströmmen lägre.

Det är i huvudsak dessa två problem som behandlas i denna doktorsavhandling:
- Hur kan solcellen byggas så att elektron-hål rekombination minskas?
- Hur kan solcellen byggas för att kunna absorbera flera fotoner?

Till exempel så undersöks i avhandlingens första artikel hur en ny typ av arbetselektrod påverkar elektron-hål rekombinationen i både elektrolyt och fastfas DSC. I avhandlingens andra, tredje och fjärde artikel så undersöks hur olika färgämnesmolekyler fungerar och påverkar funktionen av färgämnes-sensiterade solceller. Artikel fem undersöker en mer fundamental fråga, hur fastfas DSC efter tillverkning påverkas av att lagras i en syrerik atmosfär. I den sista artikeln i denna doktorsavhandling presenteras en helt ny typ av tandem solcell där en fastfas färgämnes-sensiterad solcell kombineras med en förångad organisk solcell. Genom att bygga/kombinera två solceller på varandra kan ljusabsorptionen öka och effektiviteten ökade till hela 6 %.

Acknowledgement

As in all endeavors, it is the people around you that make the journey worth taking. I would like to thank the following people for their help, support, feedback, fun and company: Professor Anders Hagfeldt, thank you for letting me do my PhD in your group, it was a challenge, it was fun and I would do it again. Also many thanks to Gerrit Boschloo, the person who helped me the most, answering my questions and questioned my ideas.

Thank you, Susanna for being a good friend and colleague, I will see you later. To Eva for all discussions and for letting me disturb you so often, you didn't disturb me, so much… Thanks Ute for watering me with ideas and suggestions, you really help me getting through. To Lei, for good collaborations and two nice summers. To the two persons that made me want to move to England: Libby, you are fun and wise, I learned a lot from you. Halina, I'll miss you.

Thank you to everyone that help me with this thesis, that are too many of you to mention, but if you feel that you deserve a pat on the back, tell me I give you a hug. To all of you that made the kitchen/lab a pleasant place to be: Sandra, Leif, Hanna, Kazu, Alex A, Xiao, Rebecka, Ulrika and Peter. I am also grateful to Erik and Håkan for helping and supporting me in my writing. Thank you Ingmar for making my stay in Germany pleasant. To the people at KTH, it is always interesting and fun to meet you guys.

To my all my friends which live both nearby and far away.

Ett speciellt tack till mina föräldrar, Jan och Ingmari som har funnits där och stöttat mig igenom alla år. Till min kära syster och bror, Frida och Robin. Min Familj, jag träffar er inte tillräckligt.

References

1 *IEA World Energy Statistic and Balances 2010*, International Energy Agency, OECD publishing, Paris, France, **2010**.

2 *IPCC Fourth Assessment Report - Climate Change 2007*, Intergovernmental Panel on Climate Change, United Nation, New York, US, **2007**.

3 *Renewables 2011: Global Status Report*, Renewable Energy Policy Network for the 21st Century, Paris, France, **2011**.

4 The average solar constant 1367 Wm^{-2} falling on earth with an area of $A=\pi R^2$. Assuming the earth area exposed to the sun as $A=4\pi R^2/2$ gives an irradiation of 684 Wm^{-2}. 30% of the light is reflected by the atmosphere and with 6-12 hrs day light yields and average 3-6 kWh $day^{-1}m^{-2}$. Electrical energy need is $2 \cdot 10^{16}$ Wh $year^{-1}$ / 365 days. 10% efficient solar cells let us convert 450 kWh day^{-1} m^{-2} resulting in an area of $1.2 \cdot 10^5$ km^2.

5 *American Society for Testing: Terrestrial Reference Spectra for Photovoltaic Performance Evaluation (ASTM G-173-03)*, National Renewable Energy Laboratory, Boulder, US, viewed Feb. 12 **2010**, http://rredc.nrel.gov/solar/spectra/am1.5/

6 A. E. Becquerel *Compt. Rend. Acad. Sci.* **1839**, *9*, 561.

7 M. A. Green Prog. Photovolt: Res. Appl. **2009**, 17, 183.

8 M. A. Green, K. Emery, Y. Hishikawa, W. Warta, E. D. Dunlop *Prog. Photovolt: Res. Appl.* **2011**, *19*, 565.

9 A. Goetzberger, C. Hebling, H.-W. Schock *Mater. Sci. Eng. Rev.* **2003**, *40*, 1.

10 K. Petritsch, PhD Thesis, Graz University of Technology, **2000.**

11 H. Hoppe, N. S. Sariciftci *J. Mater. Res.* **2004**, *19*, 1924.

12 I. Bruder, PhD Thesis, University of Stuttgart, **2010.**

13 B. O'Regan, M. Grätzel *Nature* **1991**, *353*, 737.

14 M. Grätzel J. Photochem. Photobiol., C **2003**, 4, 145.

15 H. J. Snaith, L. Schmidt-Mende *Adv. Mater.* **2007**, *19*, 318.

16 J. M. Kroon, H. J. Bakker, H. J. P. Smit, P. Liska, K. R. Thampi, P. Wang, S. M. Zakeeruddin, M. Grätzel, A. Hinsch, S. Hore, U. Würfel, R. Sastrawan, J. R. Durrant, E. Palomares, H. Pettersson, T. Gruszecki, J. Walter, K. Skupien, G. E. Tulloch *Prog. Photovolt: Res. Appl.* **2007**, *15*, 1.

17 C. S. Karthikeyan, M. Thelakkat *Inorg. Chim. Acta* **2008**, *361*, 635.

18 J.-H. Yum, P. Chen, M. Grätzel, M. K. Nazeeruddin *Chem. Sus. Chem.* **2008**, *1*, 699.

19 L. M. Peter *Phys. Chem. Chem. Phys.* **2007**, *9*, 2630.

20 A. Hagfeldt, M. Grätzel *Chem. Rev.* **1995**, *95*, 49.

21 E. L. Unger, E. Ripaud, P. Leriche, A. Cravino, J. Roncali, E. M. J. Johansson, A. Hagfeldt, G. Boschloo *J. phys. Chem. C* **2010**, *114*, 11659.

22 A. Yella, H.-W. Lee, H. N. Tsao, C. Yi, A. K. Chandiran, M. K. Nazeeruddin, E. W.-G. Diau, C.Y. Yeh, S. M. Zakeeruddin, M. Grätzel *Science* **2011**, *334*, 629.

23 A. Hagfeldt, G. Boschloo, L. Sun, L. Kloo, H. Pettersson *Chem. Rev.* **2010**, *110*, 6595.
24 H. Gerischer *Surf. Sci.* **1969**, *18*, 97.
25 R. A. Marcus *Annu. Rev. Phys. Chem.* **1964**, *15*, 155.
26 W. M. Haynes, *CRC Handbook of Chemistry and Physics*, 92nd Ed. (Internet Version), CRC Press/Taylor and Francis: Boca Raton, US, **2011**.
27 U. Bach, D. Lupo, P. Comte, J. E. Moser, F. Weissörtel, J. Salbeck, H. Spreitzer, M. Grätzel *Nature* **1998**, *395*, 583.
28 N.Cai, S.-J. Moon, L. Cevey-Ha, T. Moehl, R. Humphry-Baker, P. Wang, S. M. Zakeeruddin, M. Grätzel *Nano Letters* **2011**, *11*, 1452.
29 J. Burschka, A. Dualeh, F. Kessler, E. Baranoff, N.-L. Cevey-Ha, C. Yi, M. K. Nazeeruddin, M. Grätzel *J. Am. Chem. Soc.* **2011**, *45*, 18042.
30 M. Boucharef, C. D. Din, M. S. Boumaza, M. Colas, H. J. Snaith, B. Ratier, J. Bouclé *Nanotechnology* **2010**, *21*, 205203.
31 L. Kavan, M. Grätzel, S.E. Gilbert, C. Klemenz, H.J. Scheel *J. Am. Chem. Soc.* **1996**, *118*.
32 D. Duonghong, J. Ramsden, M. Grätzel *J. Am. Chem. Soc.* **1982**, *104*.
33 U. Diebold *Surf. Sci. Rep.* **2003**, *48*, 53.
34 C. J. Barbé, F. Arendse, P. Comte, M. Jirousek, F. Lenzmann, V. Shklover, M. Grätzel *J. Am. Ceram. Soc* **1997**, *80*, 3157.
35 A. D. McNaught, A. Wilkinson *IUPAC. Compendium of Chemical Terminology*, 2nd Ed, Blackwell Scientific Publications: Oxford, UK, **1997.**
36 S. Brunauer, P. H. Emmett, E. Teller *J. Am. Chem. Soc.* **1938**, *60*, 309.
37 P. J. Cameron, L. M. Peter *J. Phys. Chem. B* **2003**, *107*, 14394.
38 B. Peng, G. Jungmann, C. Jäger, D. Haarer, H.-W. Schmidt, M. Thelakkat *Coord. Chem. Rev.* **2004**, *248*, 1479.
39 U. Bach, PhD Thesis, Ècole polytechnique Fédérale de Lausanne, **2000.**
40 L. Kavan, M. Grätzel *Electrochem. Acta* **1995**, *40*, 643.
41 H. J. Snaith, A. J. Moule, C. Klein, K. Meerholtz, R. H. Friend, M. Grätzel *Nano Letters* **2007**, *7*, 3372.
42 I. J. Kramer, A. G. Pattantyus-Abraham, A. R. Barkhouse, X. Wang, G. Konstantatos, R. Debnath, L. Levina, I. Raabe, M. K. Nazeeruddin, M. Grätzel, E. H. Sargent *Thin Solid Films* **2011**, *519*, 7351.
43 P. Wang, C. Klein, R. Humphry-Baker, S. M. Zakeeruddin, M. Grätzel *J. Am. Chem. Soc.* **2005**, *127*, 808.
44 L. Schmidt-Mende, U. Bach, R. Humphry-Baker, T. Horiuchi, H. Miura, S. Ito, S. Uchida, M. Grätzel *Adv. Mater.* **2005**, *17*, 813.
45 K. Murakoshi, G. Kano, Y. Wada, S. Yanagida, H. Miyazaki, M. Masumoto, S. Murasawa *J. Electroanal. Chem.* **1995**, *396*, 27.
46 C. P. León, L. Kador, B. Peng, M. Thelakkat *J. Phys. Chem. B* **2006**, *110*, 8723.
47 T. Horiuchi, H. Miura, S. Uchida *Chem. Commun.* **2003**, 3036.
48 A. J. Bard, L. R. Faulkner *Electrochemical methods: Fundamentals and application*; 2nd Ed, John Wiley & Sons: Hoboken, US, **2001.**
49 G. Boschloo, A. Hagfeldt *Acc. Chem. Res.* **2009**, *42*, 1819.
50 Y. Chiba, A. Islam, Y. Watanabe, R. Komiya, N. Koide, L. Han *Jp. J. Appl. Phys.* **2006**, *45*, 638.
51 T. Daeneke, T-H. Kwon, A. B. Holmes, N. W. Duffy, U. Bach, L. Spiccia *Nat. Chem.* **2011**, *3*, 211.
52 M. Wang, N. Chamberland, L. Breau, J.-E. Moser, R. Humphry-Baker, B. Marsan, S. M. Zekeeruddin, M. Gräzel *Nat. Chem.* **2010**, *2*, 385.
53 D. Poplavskyy, J. Nelson *J. Appl. Phys.* **2003**, *93*, 341.

54 R. Pudzich, T. Fuhrmann-Lieker, J. Salbeck *Adv. Polym. Sci.* **2006**, *199*, 83.
55 Q.-B. Meng, K. Takahashi, X.-T. Zhang, I. Sutanto, T. N. Rao, O. Sato, A. Fujishima *Langmuir* **2003**, *19*, 3572.
56 B. O'Regan, D. T. Schwartz *J. Appl. Phys.* **1996**, *80*, 4749.
57 K. Tennakone, A. R. Kumarasinghe, P. M. Sirimanne, G. R. R. A. Kumara *Thin Solid Films* **1995**, *261*, 307.
58 R. Zhu, C.-Y. Jiang, B. Liu, S. Ramakrishna *Adv. Mater.* **2009**, *21*, 994.
59 X. Liu, W. Zhang, S. Uchida, L. Cai, B. Liu, S. Ramakrishna *Adv. Mater.* **2010**, *22*, 150.
60 J. Li, T. Osasa, Y. Hirayama, T. Sano, K. Wakisaka, M. Matsumura *Jp. J.Appl. Phys.* **2006**, *45*, 8728.
61 E. M. J. Johansson, S. Pradhan, E. Wang, E. L. Unger, A. Hagfeldt, M. R. Andersson *Chem. Phys. Lett.* **2011**, *502*, 225.
62 Y. Zhao, W. Chen, J. Zhai, X. Sheng, Q. He, T. Wei, F. Bai, L. Jiang, D. Zhu *Chem. Phys. Lett.*. **2007**, *445*, 259.
63 M. Karlsson unpublished work, Dept. Chemistry, Uppsala University, Sweden, 2008-2012.
64 P. Strohriegl, J. V. Grazulevicius *Adv. Mater.* **2002**, *14*, 1439.
65 Y. Shirota, H. Kageyama *Chem. Rev.* **2007**, *107*, 953.
66 T. P. I Saragi, T. Fuhrmann-Lieker, J. Salbeck *Adv. Func. Mater.* **2006**, *16*, 966.
67 U. Bach, K. De Cloedt, H. Spreitzer, M. Grätzel *Adv. Mater.* **2000**, *12*, 1060.
68 P. M. Sommeling, B. C. O'Regan, R. R. Haswell, H. J. P. Smit, N. J. Bakker, J. J. T. Smits, J. M. Kroon, J. A. M. van Roosmalen *J. phys. Chem. B* **2006**, *110*, 19191.
69 B. C. O'Regan, J. R. Durrant, P. M. Sommeling, N. J. Bakker *J. Phys. Chem. B* **2007**, *111*, 14001.
70 C. Shi, S. Dai, K. Wang, X. Pan, F. Kong, L. Hu *Vib. Spectr.* **2005**, *39*, 99..
71 G. Boschloo, L. Häggman, A. Hagfeldt *J. Phys. Chem. B* **2006**, *110*, 13144.
72 W. H. Howie, J. E. Harris, J. R. Jennings, L. M. Peter *Sol. Energy Mater. Sol. Cells* **2007**, *2007*, 424.
73 Y. Liu, A. Hagfeldt, X.-R. Xiao, S.-E. Lindquist *Sol. Energy Mater. Sol. Cells* **1998**, *55*, 267.
74 S. A. Haque, T. Park, C. Xu, S. Koops, N. Schulte, R. J. Potter, A. B. Holmes, J. R. Durrant *Adv. Func. Mater.* **2004**, *14*, 435.
75 A. Zaban, A. Meier, B. A. Gregg *J. Phys. Chem. B* **1997**, *101*, 7985.
76 S. Pelet, J.-E. Moser, M. Grätzel *J. Phys. Chem. B* **2000**, *104*, 1791.
77 H. J. Snaith, M. Grätzel *Appl. Phys. Lett.* **2006**, *89*, 2621141.
78 Z.-S. Wang, Y. Cui, Y. Dan-oh, C. Kasada, A. Shinpo, K. Hara *J. Phys. Chem. C* **2007**, *2007*, 7224.
79 T. Marinado, M. Halin, X. Jiang, M. Quintana, E. M. J. Johansson, E. Gabrielsson, S. Plogmaker, D. P. Hagberg, G. Boschloo, S. M. Zakeeruddin, M. Grätzel, H. Siegbahn, L. Sun, A. Hagfeldt, H. Rensmo *J. Phys. Chem. C* **2010**, *114*, 11903.
80 A. Allegrucci, N. A. Lewcenko, A. J. Moser, L. Dennany, P. Wagner, D. L. Officer, K. Sunahara, S. Mori, L. Spiccia *Energy Environ. Sci.* **2009**, *2*, 1069.
81 P. Wang, S. M. Zekeeruddin, R. Humphry-Baker, J. E. Moser, M. Grätzel *Adv. Mater.* **2003**, *15*, 2101-2104.
82 N. Papageorgiou, W. F. Maier, M. Grätzel *J. Electrochem. soc.* **1997**, *144*, 876.
83 X. Lin, M. Wu, Y. Wang, A. Hagfeldt, T. Ma *Chem. Commun.* **2011**, *47*, 11489.

84 M. Wang, A. M. Anghel, B. Marsan, N.-L. Cevey-Ha, N. Pootrakulchote, S. M. Zakeeruddin, M. Grätzel *J. Am. Chem. Soc.* **2009**, *131*, 15976.
85 T. N. Murakami, S. Ito, Q. Wang, M. K. Nazeeruddin, T. Bessho, I. Cesar, P. Liska, R. Humphry-Baker, P. Comte, P. Péchy, M. Grätzel *J. Electrochem. Soc.* **2006**, *153*, 2255.
86 J. Xia, C. Yuan, S. Yanagida *Appl. Mater. Inter.* **2010**, *2*, 2136.
87 Würfel, P. *Physics of solar cells: From principles to new concepts*; Wiley-VCH Verlag GmbH: Weinheim, Germany, **2005.**
88 J. Bisquert, D. Cahen, G. Hodes, S. Rühle, A. Zaban *J. Phys. Chem. B* **2004**, *108*, 8106.
89 T. Hannappel, B. Burfindt, W. Storck, F. Willig *J. Phys. Chem. B* **1997**, *101*, 6799.
90 R. J. Ellingson, J. B. Asbury, S. Ferrere, H. N. Ghosh, J. R. Sprague, T. Lian, A. J. Nozik *J. Phys. Chem. B* **1998**, *102*, 6455.
91 J. M. Szarko, A. Neubauer, A. Bartelt, L. Socaciu-Siebert, F. Birkner, K. Schwarzburg, T. Hannapple, R. Eichberger *J. Phys. Chem. C* **2008**, *112*, 10542.
92 S. A. Haque, Y. Tachibana, D. R. Klug, J. R. Durrant *J. Phys. Chem. B* **1998**, *102*, 1745.
93 J. N. Clifford, E. Palomares, M. K. Nazeeruddin, M. Grätzel, J. R. Durrant *J. Phys. Chem. B* **2007**, *111*, 6561.
94 D. J. Fitzmaurice, H. Frei *Langmuir* **1991**, *7*, 1129.
95 M. K. Nazeeruddin, A. Kay, I. Rodicio, R. Humphry-Baker, E. Muller, P. Liska, N. Vlachopoulos, M. Grätzel *J. Am. Chem. Soc.* **1993**, *115*, 6382.
96 B. O'Regan, J. Moser, M. Anderson, M. Grätzel *J. Phys. Chem.* **1990**, *94*, 8720.
97 A. Solbrand, H. Lindström, H. Rensmo, A. Hagfeldt, S.-E. Lindquist *J. Phys. Chem. B* **1997**, *101*, 2514.
98 J. Nelson *Phys. Rev. B* **1999**, *59*, 15374.
99 J. Bisquert, A. Zaban *Appl. Phys. A* **2003**, *77*, 507.
100 J. Bisquert, V. S. Vikhrenko *J. Phys. Chem. B* **2004**, *108*, 2313.
101 J. R. Jennings, L. M. Peter *J. Phys. Chem. C* **2007**, *111*, 16100.
102 A. C. Fischer, L. M. Peter, E. A. Ponomarev, A. B. Walker, K. G. U. Wijayantha *J. Phys. Chem. B* **2000**, *104*, 949.
103 H. K. Dunn, P.-O. Westin, D. R. Staff, L. M. Peter, A. B. Walker, G. Boschloo, A. Hagfeldt *J. Phys. Chem. C* **2011**, *115*, 13932.
104 N. Papageorgiou, M. Grätzel, P. P. Infelta *Sol. Energy Mater. Sol. Cells* **1996**, *44*, 405.
105 U. Bach, Y. Tachibana, J.-E. Moser, S. A. Haque, J. R. Durrant, M. Grätzel, D. R. Klug *J. Am. Chem. Soc.* **1999**, *121*, 7445.
106 V. Coropceanu, J. Cornil, D. A. da Silva Filho, Y. Olivier, R. Silbey, J.-L. Bredas *Chem. Rev.* **2009**, *107*, 926.
107 J. Kirkpatrick, J. Nelson *J. Chem. Phys.* **2005**, *123*, 0847031.
108 H. Bässler, P. M. Borsenberger *Chem. Phys.* **1993**, *177*, 763.
109 Bässler, H. *Phys. Stat. Solidi B.* **1993**, *175*, 15.
110 U. B. Cappel, E. A. Gibson, A. Hagfeldt, G. Boschloo *J. Phys. Chem. C* **2009**, *113*, 6275.
111 H. J. Snaith, R. Humphry-Baker, P. Chen, I. Cesar, S. M. Zakeeruddin, M. Grätzel *Nanotechnology* **2008**, *19*, 42400301.
112 N. Rossier-Iten, PhD Thesis, École polytechnique Fédérale de Lausanne, **2006**.
113 P. Tiwana, P. Docampo, M. B. Johnston, H. J. Snaith, L. M. Herz *ACS Nano* **2011**, *5*, 5158.

114 W. Shockley, H. J. Queisser *J. Appl. Phys.* **1961**, *32*, 510.
115 M. K. Nazeeruddin, F. De Angelis, S. Fantacci, A. Selloni, G. Viscardi, P. Liska, S. Ito, B. Takeru, M. Grätzel *J. Am. Chem. Soc.* **2005**, *127*, 16835.
116 H. J. Snaith *Adv. Func. Mater.* **2010**, *20*, 13.
117 S. M. Feldt, E. A. Gibson, E. Gabrielsson, L. Sun, G. Boschloo, A. Hagfeldt *J. Am. Chem. Soc.* **2010**, *132*, 16714.
118 M. Wang, P. Chen, R. Humphry-Baker, S. M. Zakeeruddin, M. Grätzel *Chem. Phys. Chem.* **2009**, *10*, 290.
119 Q. Wang, J.-E. Moser, M. Grätzel *J. Phys. Chem. B* **2005**, *109*, 14945.
120 Q. Yu, Y. Wang, Z. Yi, N. Zu, J. Zhang, P. Wang *ACS Nano* **2010**, *4*, 6032.
121 H. K. Dunn, L. M. Peter *J. Phys. Chem. C* **2009**, *113*, 4726.
122 J. Krueger, R. Plass, M. Grätzel, P. J. Cameron, L. M. Peter *J. Phys. Chem. B* **2003**, *107*, 7536.
123 J. Melas-Kyriazi, I.-K. Ding, A. Marchioro, A. Punzi, B. E. Hardin, G. F. Burkhard, N. Tétreault, M. Grätzel, J.-E. Moser, M. D. McGehee *Adv. Energy. Mater.* **2011**, *1*, 407.
124 H. J. Snaith, M. Grätzel *Adv. Mater.* **2007**, *19*, 3643.
125 I.-K. Ding, N. Tétreault, J. Brillet, B. E. Hardin, E. H. Smith, S. J. Rosenthal, F. Sauvage, M. Grätzel, M. D. McGehee *Adv. Func. Mater.* **2009**, *19*, 2431.
126 I.-K. Ding, J. Melas-Kyriazi, N.-L. Cevey-Ha, K. G. Chittibabu, S. M. Zakeeruddin, M. Grätzel, M. D. McGehee *Organic electronics* **2010**, *11*, 1217.
127 P. Wang, S. M. Zekeeruddin, J. E. Moser, M. K. Nazeeruddin, T. Sekiguchi, M. Grätzel *Nature Materials* **2003**, *2*, 402.
128 M. Wang, S.-J. Moon, M. Xu, K. Chittibabu, P. Wang, N.-L. Cevey-Ha, R. Humphry-Baker, S. M. Zakeeruddin, M. Grätzel *Small* **2010**, *6*, 319.
129 L. Yang, U. B. Cappel, E. L. Unger, M. Karlsson, K. M. Karlsson, E. Gabrielsson, L. Sun, G. Boschloo, A. Hagfeldt, E. M. J. Johansson *Phys. Chem. Chem. Phys.* **2012**, *14*, 779.
130 S. Ito, T. N. Murakami, P. Comte, P. Liska, C. Grätzel, M. K. Nazeeruddin, M. Grätzel *Thin Solid Films* **2007**, *516*, 4613.
131 S. Ito, P. Liska, P. Comte, R. Charvet, P. Péchy, U. Bach, L. Schmidt-Mende, S. M. Zakeeruddin, A. Kay, M. K. Nazeeruddin, M. Grätzel *Chem. Commun.* **2005**, 4351.
132 C. A. Grimes, O. K. Varghese, S. Ranja Light, Water, Hydrogen: The solar generation of hydrogen by water photoelectrolysis; Springer: Strassen, Luxembourg, **2008.**
133 S. G. Kwon, T. Hyeon *Acc. Chem. Res.* **2008**, *41*, 1696.
134 M. Birkholz *Thin film analysis by X-ray scattering*; Wiley-VCH Verlag GmbH: Weinheim, Germany, **2006**.
135 A. Kay, M. Grätzel *Chem. Mater.* **2002**, *14*, 2930.
136 T. W. Hamann, O. K. Farha, J. T. Hupp *J. Phys. Chem. C* **2008**, *112*, 19756.
137 T. C. Li, M. S. Góes, F. Fabregat-Santiago, J. Bisquert, P. R. Bueno, C. Prasittichai, J. T. Hupp, T. J. Marks *J. Phys. Chem. C* **2009**, *113*, 18385.
138 S. M. George *Chem. Rev.* **2010**, *110*, 111.
139 M. Leskelä, M. Ritala *Angew. Chem. Int. Ed.* **2003**, *42*, 5548.
140 J. R. Bakke, K. L. Pickrahn, T. P. Breean, S. F. Bent *Nanoscale* **2011**, *3*, 3482.
141 J. Aarik, A. Aidla, H. Mändar, T. Uustare *App. Surf. Sci.* **2001**, *172*, 148.
142 G. C. Fuentes, E. Elizalde, F. Yubero, J. M. Sanz *Surf. Inter. Anal.* **2002**, *33*, 230.
143 M. Gorgoi, S. Svensson, F. Schäfers, G. Öhrwall, M. Mertin, P. Bressler, O. Karis, H. Siegbahn, A. Sandell, W. Doherty, C. Jung, W. Braun, W. Eberhardt *Nucl. Instr. and Meth. A* **2009**, *601*, 48.

144 A. Zaban, M. Greenshtein, J. Bisquert *Chem. Phys. Chem.* **2003**, *4*, 859.
145 N. W. Duffy, L. M. Peter, R. M. G. Rajapakse, K. G. U. Wijayantha *Electrochem. Commun.* **2000**, *2*, 658.
146 Y. Fukai, Y. Kondo, S. Mori, E. Suzuki *Electrochem. Commun.* **2007**, *9*, 1439.
147 F. Fabregat-Santiago, J. Bisquert, G. Garcia-Belmonte, G. Boschloo, A. Hagfeldt *Sol. Energy Mater. Sol. Cells* **2005**, *87*, 117.
148 J. Bisquert *Phys. Chem. Chem. Phys.* **2003**, *5*, 5360.
149 S. M. Feldt, G. Wang, G. Boschloo, A. Hagfeldt *J. Phys. Chem. C*, *115*, 21500.
150 J. Wiberg, T. Marinado, D. P. Hagberg, L. Sun, A. Hagfeldt, B. Albinsson *J. Phys. Chem. B* **2010**, *114*, 14358.
151 G. Boschloo, D. Fitzmaurice *J. Phys. Chem. B* **1999**, *103*, 7860.
152 K. Rajeshwar, L. M. Peter, A. Fujishima, D. Meissner, M. Tomkiewich *Proceedings of the symposium on photoelectrochemistry*; The Electrochemical Society, Inc.; Pennington, USA, **1997**.
153 N. F. Sheppard, R. C. Tucker, C. Wu *Anal. Chem.* **1993**, *65*, 1199.
154 H. J. Snaith, L. Schmidt-Mende, M. Grätzel, M. Chiesa *Phys. Rev. B* **2006**, *74*, 045306.
155 H. Klauk *Chem. Soc. Rev.* **2010**, *39*, 2643.
156 K. C. Kao, W. Hwang *Electrical transport in solids*; Pergamon Press; Oxord, UK, **1981**.
157 G. Juska, K. Arlauskas, M. Viliunas, J. Kocka *Phys. Rev. Lett.* **2000**, *84*, 4946.
158 P. Cusumano, S. Gambino *J. Electron. Mater.* **2007**, *37*, 231.
159 S. Tiwari, N. C. Greenham *Opt. Quant. Electron.* **2009**, *41*, 69.
160 A. Fleissner, H. Schmid, C. Melzer, H. von Seggern *Appl. Phys. Lett.* **2007**, *91*, 242103.
161 R. Schmechel, H. von Seggern *Phys. Stat. Sol. A* **2004**, *201*, 1215.
162 M. Dürr, A. Yasuda, G. Nelles *Appl. Phys. Lett.* **2006**, *89*, 061110.
163 A. N. M. Green, E. Palomares, S. A. Haque, J. M. Kroon, J. R. Durrant *J. Phys. Chem. B* **2005**, *109*, 12525.
164 Q. Zhang, T. P. Chou, B. Russo, S. A. Jenekhe, G. Cao *Adv. Func. Mater.* **2008**, *18*, 1654.
165 P. Guo, M. A. Aegerter *Thin Solid Films* **1999**, *351*, 290.
166 S. Gubbala, V. Chakrapani, V. Kumar, M. K. Sunkara *Adv. Func. Mater.* **2008**, *18*, 2411.
167 J. M. Macák, H. Tsuchiya, A. Ghicov, P. Schmuki *Electrochem. Commun.* **2005**, *7*, 1133.
168 J. Qian, P. Liu, Y. Xiao, Y. Jiang, Y. Cao, X. Ai, H. Yang *Avd. Mater.* **2009**, *21*, 1.
169 K. Tennakone, G. R. R. A. Kumara, I. R. M. Kottegoda, V. P. S. Perera *Chem. Commun.* **1999**, 15.
170 S. Chappel, S.-G. Chen, A. Zaban *Langmuir* **2002**, *18*, 3336.
171 Y. Diamant, S. Chappel, S. G. Chen, O. Melamed, A. Zaban *Coord. Chem. Rev.* **2004**, *248*, 1271.
172 Y. Diamant, S. G. Chen, O. Melamed, A. Zaban *J. Phys. Chem. B* **2003**, *107*, 1977.
173 C. Prasittichai, J. T. Hupp *J. Phys. Chem. Lett.* **2010**, *1*, 1611.
174 E. Palomares, J. N. Clifford, S. A. Haque, T. Lutz, J. R. Durrant *J. Am. Chem. Soc.* **2003**, *125*, 475.
175 G. R. A. Kumara, M. Okuya, M. Murakami, S. Kaneko, V. V. Jayaweera, K. Tennakone *J. Photochem. Photobiol. B* **2004**, *164*, 183.
176 A. Cravino, P. Schilinsky, C. J. Brabec *Adv. Func. Mater.* **2007**, *17*, 3906.

177 D. P. Hagberg, T. Edvinsson, T. Marinado, G. Boschloo, A. Hagfeldt, L. Sun *Chem. Commun.* **2006**, 2245-.
178 D. P. Hagberg, J.-H. Yum, H. Lee, F. De Angleis, T. Marinado, K. M. Karlsson, R. Humphry-Baker, L. Sun, A. Hagfeldt, M. Grätzel, M. K. Nazeeruddin *J. Am. Chem. Soc.* **2008**, *130*, 6259.
179 D. P. Hagberg, X. Jiang, E. Gabrielsson, M. Linder, T. Marinado, T. Brinck, A. Hagfeldt, L. Sun *J. Mater. Chem.* **2009**, *19*, 7232.
180 A. Abbotto, N. Manfredi, C. Marinzi, F. De Angelis, E. Mosconi, J.-H. Yum, Z. Xianxi, M. K. Nazeeruddin, M. Grätzel *Energy Environ. Sci.* **2009**, *2*, 1094.
181 T. Marinado, PhD Thesis, Royal Institute of Technology, **2009**.
182 A. Dubois, M. Canva, A. Brun, F. Chaput, J.-P. Boilot *Appl. Opt.* **1996**, *35*, 3193.
183 T. Weil, T. Vosch, J. Hofkens, K. Peneva, K. Mullen *Angew. Chem. Int. Ed.* **2010**, *49*, 9068.
184 Y. Shibano, T. Umeyama, Y. Matano, H. Imahori *Org. Lett.* **2007**, *9*, 1971.
185 T. Edvinsson, C. Li, N. Pschirer, J. Schneboom, F. Eickemeyer, R. Sens, G. Boschloo, A. Herrmann, K. Muellen, A. Hagfeldt *J. Phys. Chem. C* **2007**, *111*, 15137.
186 C. Li, Z. Liu, J. Schöneboom, F. Eickemeyer, N. G. Pschirer, P. Erk, A. Herrmann, K. Mullen *J. Mater. Chem.* **2009**, *19*, 5405.
187 U. Cappel, PhD Thesis, Uppsala University, **2011**.
188 U. B. Cappel, S. Plogmaker, E. M. J. Johansson, A. Hagfeldt, G. Boschloo, H. Rensmo *Phys. Chem. Chem. Phys.* **2011**, *13*, 14767.
189 U. B. Cappel, A. L. Smeigh, S. Plogmaker, E. M. J. Johansson, H. Rensmo, L. Hammarström, A. Hagfeldt, G. Boschloo *J. Phys. Chem. C* **2011**, *115*, 4345.
190 T. G. Pavlopoulos *Appl. Opt.* **1997**, *36*, 4969.
191 B. C. Channu, H. N. Kalpana, G. B. Eregowda, C. Dass, P. J. Houghton, K. N. Thimmaiah *J. Pharm. Biomed. Anal.* **1999**, *21*, 775.
192 H. Tian, I. Bora, X. Jiang, E. Gabrielsson, K. M. Karlsson, A. Hagfeldt, L. Sun *J. Mater. Chem.* **2011**, *21*, 12462.
193 H. Tian, X. Yang, J. Cong, R. Chen, J. Liu, Y. Hao, A. Hagfeldt, L. Sun *Chem. Commun.* **2009**, 6288.
194 K. M. Karlsson, X. Jiang, S. K. Eriksson, E. Gabrielsson, H. Rensmo, A. Hagfeldt, L. Sun *Chem. Eur. J.* **2011**, *17*, 6415.
195 F. Fabregat-Santiago, J. Bisquert, L. Cevey, P. Chen, M. Wang, S. M. Zakeeruddin, M. Grätzel *J. Am. Chem. Soc.* **2009**, *131*, 558.
196 P. Docampo, H. J. Snaith *Nanotechnology* **2011**, *22*, 225403.
197 J. Y. Kim, K. Lee, N. E. Coates, D. Moses, T.-Q. Nguyen, M. Dante, A. J. Heeger *Science* **2007**, *317*, 222.
198 L. A. A. Pettersson, L. S. Roman, O. Inganäs *J. Appl. Phys.* **1999**, *86*, 487.
199 K. Fredin, E. M. J. Johanson, T. Blom, M. Hedlund, S. Plogmaker, H. Siegbahn, K. Leifer, H. Rensmo *Synth. Met.* **2009**, *159*, 166.

Acta Universitatis Upsaliensis

Digital Comprehensive Summaries of Uppsala Dissertations from the Faculty of Science and Technology 892

Editor: The Dean of the Faculty of Science and Technology

A doctoral dissertation from the Faculty of Science and Technology, Uppsala University, is usually a summary of a number of papers. A few copies of the complete dissertation are kept at major Swedish research libraries, while the summary alone is distributed internationally through the series Digital Comprehensive Summaries of Uppsala Dissertations from the Faculty of Science and Technology.

Distribution: publications.uu.se
urn:nbn:se:uu:diva-165458

ACTA
UNIVERSITATIS
UPSALIENSIS
UPPSALA
2012